ANL/ESD/12-13

Computational Mechanics Research and Support for Aerodynamics and Hydraulics at TFHRC, Year 2 Quarter 1 Progress Report

Energy Systems Division

About Argonne National Laboratory
Argonne is a U.S. Department of Energy laboratory managed by UChicago Argonne, LLC under contract DE-AC02-06CH11357. The Laboratory's main facility is outside Chicago, at 9700 South Cass Avenue, Argonne, Illinois 60439. For information about Argonne and its pioneering science and technology programs, see www.anl.gov.

Availability of This Report
This report is available, at no cost, at http://www.osti.gov/bridge. It is also available on paper to the U.S. Department of Energy and its contractors, for a processing fee, from:

U.S. Department of Energy
Office of Scientific and Technical Information
P.O. Box 62
Oak Ridge, TN 37831-0062
phone (865) 576-8401
fax (865) 576-5728
reports@adonis.osti.gov

ANL/ESD/12-13

Computational Mechanics Research and Support for Aerodynamics and Hydraulics at TFHRC, Year 2 Quarter 1 Progress Report

by
S.A. Lottes[1], C. Bojanowski[1], J. Shen[2], Z. Xie[2], and Y. Zhai[2]
[1] Transportation Research and Analysis Computing Center (TRACC)
Energy Systems Division, Argonne National Laboratory
[2] Turner-Fairbank Highway Research Center

February 2012

Argonne NATIONAL LABORATORY

Computational Mechanics Research and Support for Aerodynamics and Hydraulics at **TFHRC**

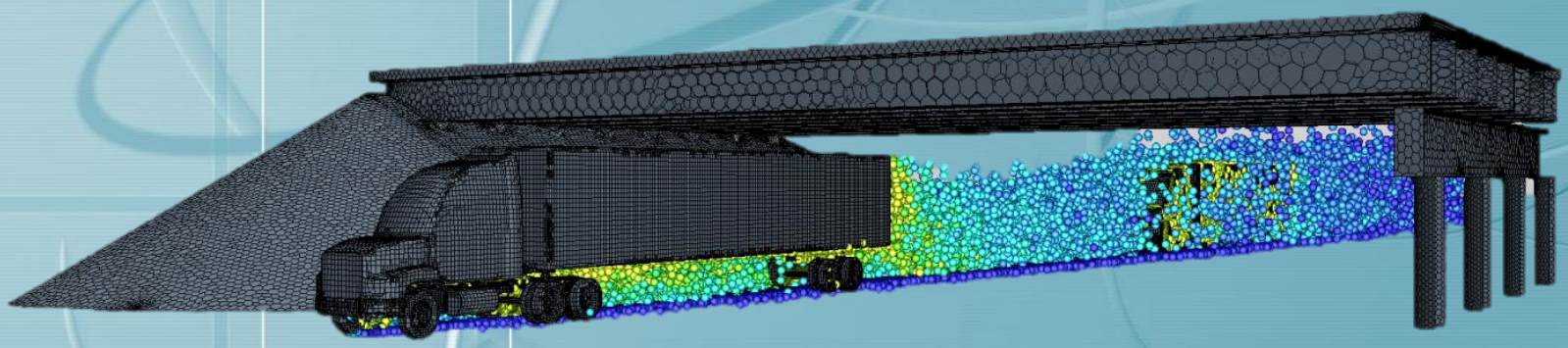

Quarterly Report

October through December 2011

Y2Q1

Computational Mechanics Research and Support for Aerodynamics and Hydraulics at TFHRC
Year 2 Quarter 1 Progress Report

Energy Systems Division (ES)
Argonne National Laboratory (ANL)

Principal Investigator:
Steven A. Lottes, Ph.D.
Argonne National Laboratory

Contributors:
Cezary Bojanowski, Ph.D.
Argonne National Laboratory

Jerry Shen, Ph.D.
Zhaoding Xie, Ph.D.
Turner-Fairbank Highway Research Center

Yuan Zhai
University of Nebraska

Submitted to:
Federal Highway Administration

Kornel Kerenyi, Ph.D.
Turner-Fairbank Highway Research Center
Federal Highway Administration
6300 Georgetown Pike
McLean, VA 22101

Harold Bosch, Ph.D.
Turner-Fairbank Highway Research Center
Federal Highway Administration
6300 Georgetown Pike
McLean, VA 22101

February 2012

Table of Contents

List of Figures

List of Tables

1. Introduction and Objectives

The computational fluid dynamics (CFD) and computational structural mechanics (CSM) focus areas at Argonne's Transportation Research and Analysis Computing Center (TRACC) initiated a project to support and compliment the experimental programs at the Turner-Fairbank Highway Research Center (TFHRC) with high performance computing based analysis capabilities in August 2010. The project was established with a new interagency agreement between the Department of Energy and the Department of Transportation to provide collaborative research, development, and benchmarking of advanced three-dimensional computational mechanics analysis methods to the aerodynamics and hydraulics laboratories at TFHRC for a period of five years, beginning in October 2010. The analysis methods employ well-benchmarked and supported commercial computational mechanics software. Computational mechanics encompasses the areas of Computational Fluid Dynamics (CFD), Computational Wind Engineering (CWE), Computational Structural Mechanics (CSM), and Computational Multiphysics Mechanics (CMM) applied in Fluid-Structure Interaction (FSI) problems.

The major areas of focus of the project are wind and water effects on bridges — superstructure, deck, cables, and substructure (including soil), primarily during storms and flood events — and the risks that these loads pose to structural failure. For flood events at bridges, another major focus of the work is assessment of the risk to bridges caused by scour of stream and riverbed material away from the foundations of a bridge. Other areas of current research include modeling of flow through culverts to improve design allowing for fish passage, modeling of the salt spray transport into bridge girders to address suitability of using weathering steel in bridges, CFD analysis of the operation of the wind tunnel in the TFHRC wind engineering laboratory.

This quarterly report documents technical progress on the project tasks for the period of October through December 2011.

1.1. Computational Fluid Dynamics Summary

The primary Computational Fluid Dynamics (CFD) activities during the quarter concentrated on the development of models and methods needed to continue the ongoing work in scour modeling, culvert modeling, CFD analysis of the Turner-Fairbank wind tunnel, CFD modeling and analysis of salt spray from

large trucks passing under bridges using weathering steel, and modeling and analysis of concept testing for an in-situ scour device to measure scour related properties of sediment bed material. During this quarter, modeling and analysis of the separation of flow at the leading edge of a flooded bridge deck was continued to aid in the development of an enhanced approach for evaluating scour due to submergence of bridge decks during floods in the federal guidelines. Modeling of flow through culverts for fish passage continued with the work on a porous media model to capture the effects of large diameter gravel in the bottom of the culvert revealed some difficulties in obtaining physically realistic results in the modeling of flow parallel to porous beds. Modeling of the wind tunnel in the TFHRC laboratory continued, and a new CFD model was developed to analyze flow in the wind tunnel and the room under a variety of flow conditions including with and without furniture. Work on the CFD model using the sliding mesh capabilities of STAR-CCM+ with multiphase droplet tracking was continued. Simulations for a matrix of conditions are being carried out with different droplet sizes, both a single truck and a truck followed by another truck, and two wind speeds with the wind crossing the domain in four directions with respect to the truck or trucks.

2. Computational Fluid Dynamics for Hydraulic and Aerodynamic Research

During the first quarter of 2012, modeling and analysis of the separation of flow at the leading edge of a flooded bridge deck was continued to aid in the development of an enhanced approach for evaluating scour due to submergence of bridge decks during floods. Modeling of flow through culverts for fish passage continued with work on using a porous media model to capture the effects of large diameter gravel in the bottom of the culvert. TFHRC provided geometry files for their wind tunnel laboratory and the new CFD model was used to analyze flow in the wind tunnel and the room under a variety of flow conditions including with and without furniture. The CFD model using the sliding mesh capabilities of STAR-CCM+ with multiphase droplet tracking is being used to test the effects of a variety of conditions of droplet distributions under bridges.

2.1. CFD Analysis of Flow Separation under an Inundated Bridge Deck for Application to Pressure Scour Evaluation

An update to the submerged-flow bridge scour evaluation procedure in HEC-18 [1] is being prepared by TFHRC. The approach to scour hole estimation assumes that the scour process will enlarge the area under the bridge until it is large enough to pass the flow with a condition of critical shear stress at the bed. The bridge deck is a bluff body in the flow and flow separation will normally occur at the upstream bottom edge of the submerged bridge deck. The separation zone under the bridge restricts the area open to flow under the deck and is therefore an important parameter in conservatively predicting the depth of the scour hole. A set of CFD simulations were performed to investigate the relation between the initial opening height under the submerged deck before scour and the thickness of the separation zone, and one test was done to see if the thickness of the separation zone changed during the scour process.

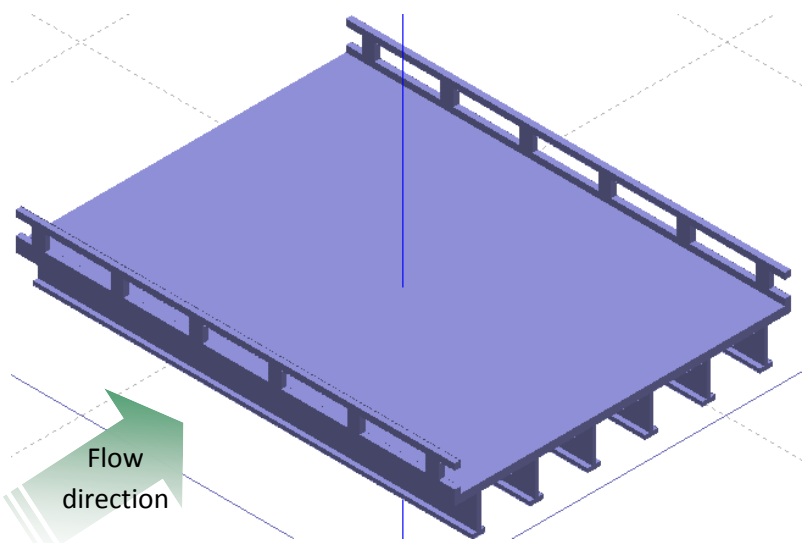

Figure 2.1: Bridge deck geometry

The bridge deck geometry is shown in Figure 2.1, and a schematic of the flow domain is shown in Figure 2.2. To reduce computer time and eliminate the effects of the flume side walls, the simulations were performed using a section of the bridge deck cut through the middle of a post and running half the distance to the center of the next post. This geometry is shown in Figure 2.3.

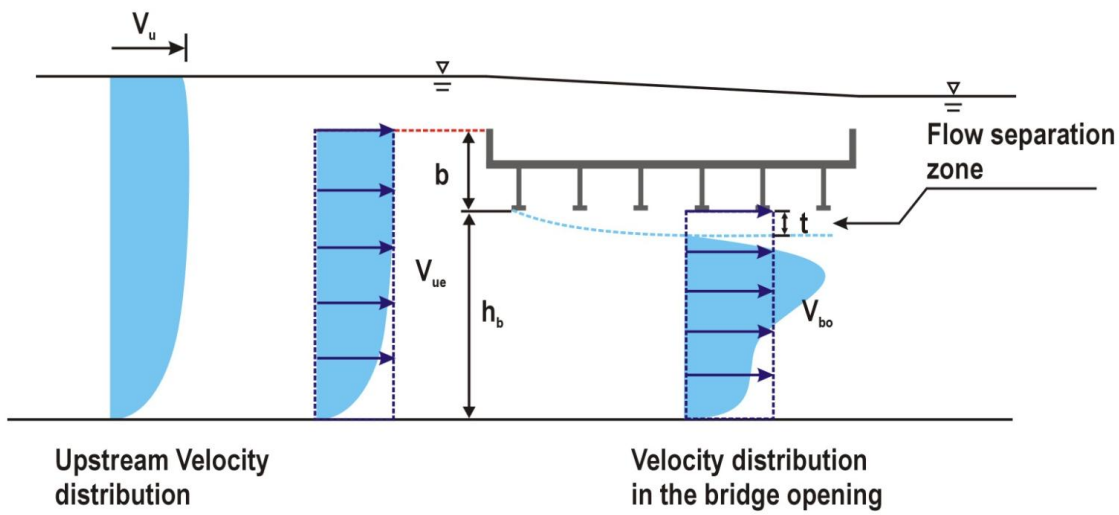

Figure 2.2: Schematic of flow domain for separation zone simulations

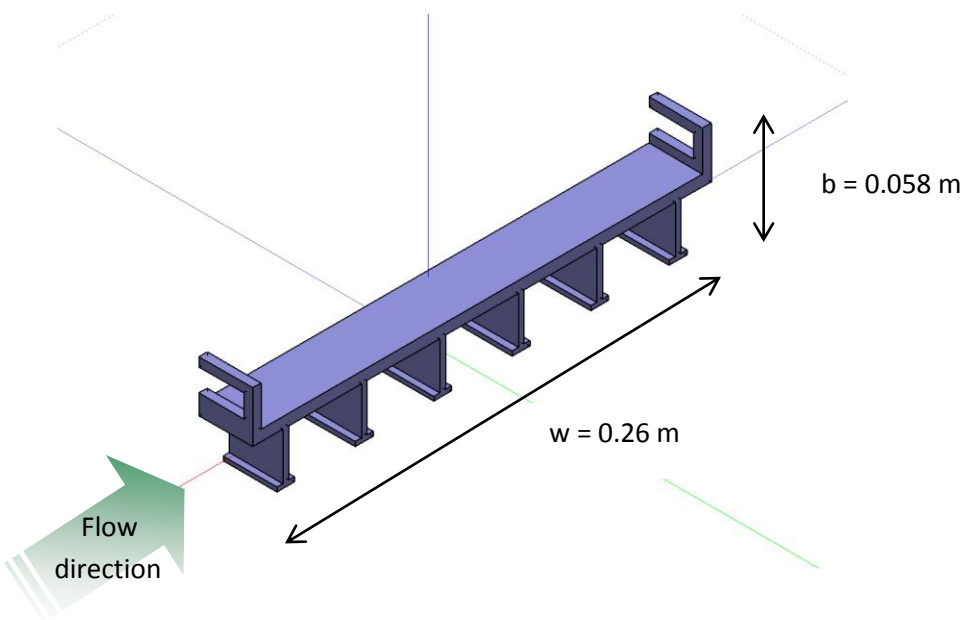

Figure 2.3: Symmetric section of bridge deck from center of a railing post to halfway to the next post

Symmetric boundary conditions were used on the cross stream sides of the domain. The simulations were done as single phase flow with a flat water surface using a symmetry boundary condition at the surface. Previous tests have been done using the multiphase VOF model for free surface flow, and the

flat surface assumption is good except in the case with the bridge deck very close to the surface but still overtopped. The inlet boundary was taken to be a uniform velocity located just at the outlet of the honeycomb in the TFHRC scour flume. The honeycomb is a flow straightener that also strips off boundary layers, and therefore the uniform inlet velocity is a reasonably good assumption applied at this position.

2.1.1. Parameters Affecting Separation Zone Maximum Thickness under Bridge Deck

The thickness of the separation zone under a flooded bridge deck, t, is affected by several factors, such as the geometry of the superstructure, constriction of the flow, bridge opening, water level, etc. Some of these parameters directly reflect the effect of the two boundaries, channel bottom and water surface in open channel flow. Thus, it is necessary to catalog different conditions based on the relative position of bridge structures to those two boundaries. The conditions include: (1) Water surface is far enough above the deck not to significantly affect the water flow conditions near the fully-submerged bridge deck. Under this flow condition, the finite distance from the bridge deck to the channel bottom is an important parameter that is related to the thickness of the separation zone, t. This is hereafter referred to as the surface-far-field condition. (2) The channel bottom is far from the bridge deck. The boundary of water surface becomes a primary factor influencing the separation zone thickness. This will be referred to as the bottom-far-field condition. (3) There is no influence from either of the boundaries to the flow field around bridge structures, which can be called the far-field condition. (4) Both of the boundaries may limit the flow field near bridge structures, which can be called the shallow water condition. Under this condition, neither surface-distance nor bottom-distance can be neglected in the analysis.

Most situations during an overtopping flood event fall into the condition (2) and (4). This also includes the partially submerged situation. To consider the condition (2) firstly, the variables that influence the thickness of separation zone, t, may be gravitational acceleration, g, water dynamic viscosity, μ, water density, ρ, surface distance, h_t, effective blocked flow rate, q_b, and overhang-geometrical factor, α, as illustrated in Figure 2.4. For a partially submerged deck, the flow between the bottom face of girders and water surface are blocked by the deck. For fully inundated deck, the blockage extends from the bottom face of girders to the highest point of the stagnation streamline. Based on a series of CFD simulations, the highest point of the stagnation streamline is found to be at approximately 10% of deck thickness (0.1T) above the upper edge of the deck blockage not including railing and posts. This maximum position of the stagnation streamline may be a combination of additional flow resistance from posts and railing and conditions where the bridge superstructure is near the water surface with flow surface level prevented from exceeding the flat surface assumption used to allow use of a single phase model. These results should be checked using the more computationally expensive two phase VOF free surface model.

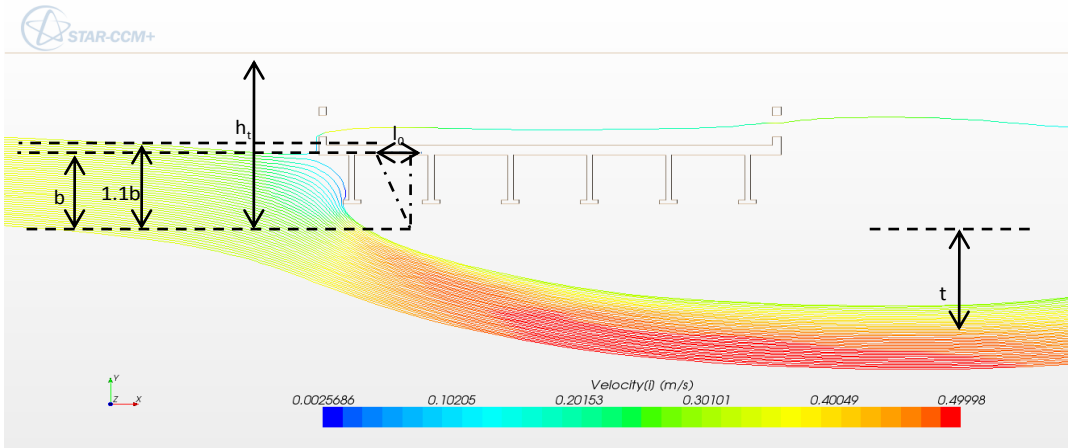

Figure 2.4: Streamlines showing the mass flow blocked by the bridge superstructure

2.1.2. Relation between Separation Zone Thickness and Bridge Width

To consider the flow condition (4) described in section 2.1.1, cases without scour are simulated in STAR-CCM+. Results showed that the separation zone thickness is dependent on bridge opening h_b and independent of the mean velocity upstream. The velocity range tested as shown in Figure 2.5. It linearly increases as bridge opening increases in a completely submerged situation, and linearly decreases as bridge opening increases, blocking less flow, in a partially submerged situation. The peak point in Figure 2.5 corresponds to the situation that the top of bridge just touches the water surface. The CFD result data for these parameters is listed in Table 2.1.

Although an obvious trend is not observed between the separation zone thickness and mean velocity upstream for the unscoured bottom, a relationship may exist for a scoured bottom contour. because the mean velocity upstream affects opening height required to pass the flow under the bridge at the critical velocity of sediment transport.

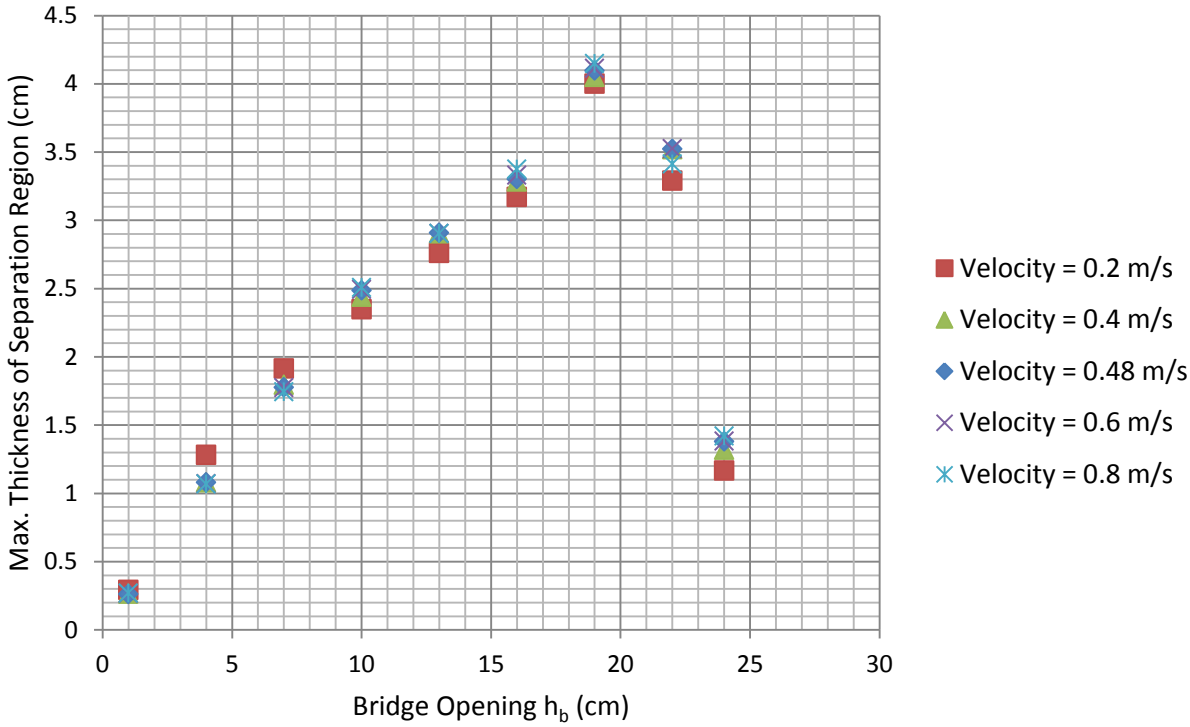

Figure 2.5: Separation Zone Thickness Verse Bridge Opening

Table 2.1: Contraction of flow under bridge deck

h_b (m)	t V_u = 0.2 m/s (m)	t V_u = 0.4 m/s (m)	t V_u = 0.48 m/s (m)	t V_u = 0.6 m/s (m)	t V_u = 0.8 m/s (m)
0.01	0.292	0.264	0.261	0.266	0.268
0.04	1.281	1.081	1.079	1.071	1.069
0.07	1.915	1.794	1.776	1.774	1.744
0.10	2.347	2.44	2.487	2.493	2.507
0.13	2.76	2.903	2.909	2.903	2.904
0.16	3.17	3.284	3.302	3.33	3.374
0.19	4	4.05	4.096	4.114	4.148
0.22	3.29	3.521	3.523	3.526	3.412
0.24	1.167	1.32	1.381	1.382	1.42

2.1.3. Relation between Separation Zone Thickness and Deck Thickness

For the bottom-far-field condition, the separation zone thickness linearly increases as deck thickness or girder length as shown in Figure 2.6 based on the numerical simulation. Qualitatively speaking, the thicker the bridge deck is, the larger the turning angle for fluid traveling along the stagnation streamline, and therefore, a greater separation zone thickness is expected.

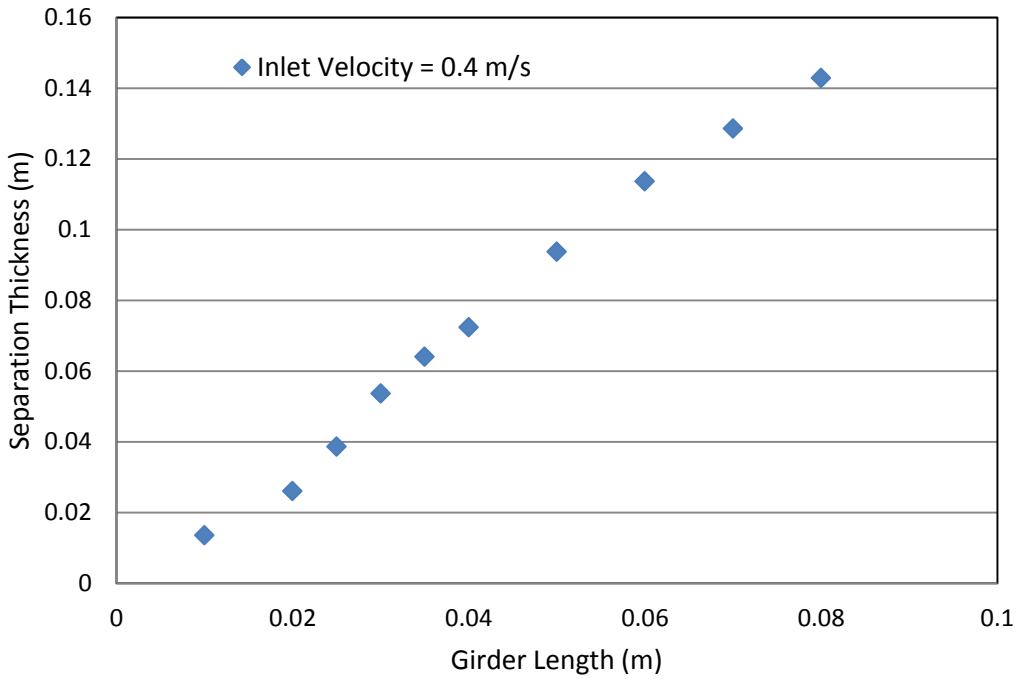

Figure 2.6: Separation Zone Thickness versus Girder length

2.1.4. Relation between Separation Zone Thickness and 1st Girder Setback

It is also found that the thickness of separation decreases as α, defined as l_o/b, increases for a given flow condition, with an approximate relationship of $t \propto e^{-\alpha}$. The relation is as shown in Figure 2.7. The effect of α may highly depend on details of bridge geometry. For the deck geometry considered in this study, the thickness of separation for different distances of setback may be obtained by multiplying the factor $e^{-\alpha_k+\alpha_0}$ by the t value based on the standard bridge deck, in which α_0 is for the standard bridge deck model with the value of 0.69, and α_k is a current ratio of overhang distance to girder length. Figure 2.8 shows the typical results for two different setbacks. With larger set back distances, the smaller blockage of the leading edge of the deck starts the turning of streamlines at a greater distance from the main blockage of the girders, yielding a smaller turning angle when the flow separates at the leading edge of the first girder and a less thick separation zone under the girders.

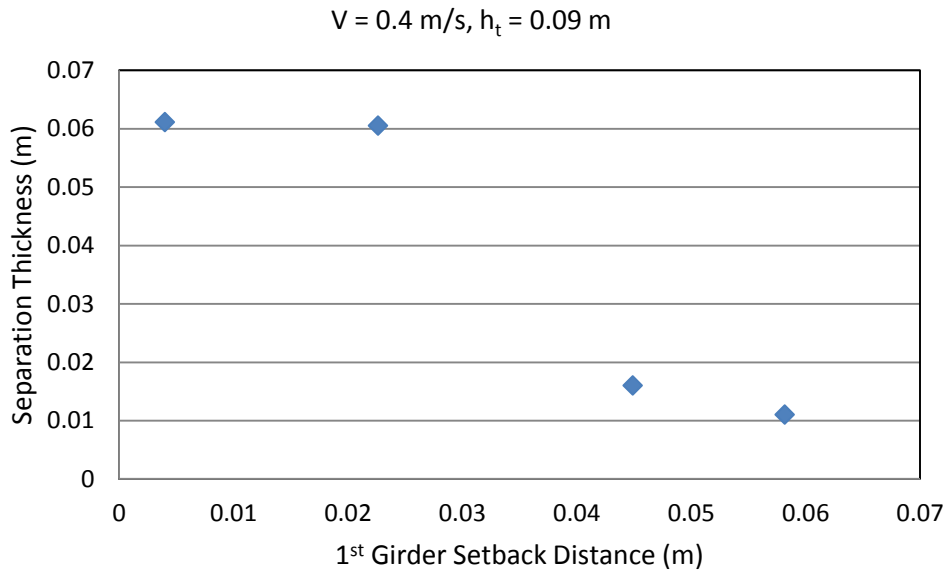

Figure 2.7: Separation Zone Thickness versus 1st Girder Setback Distance

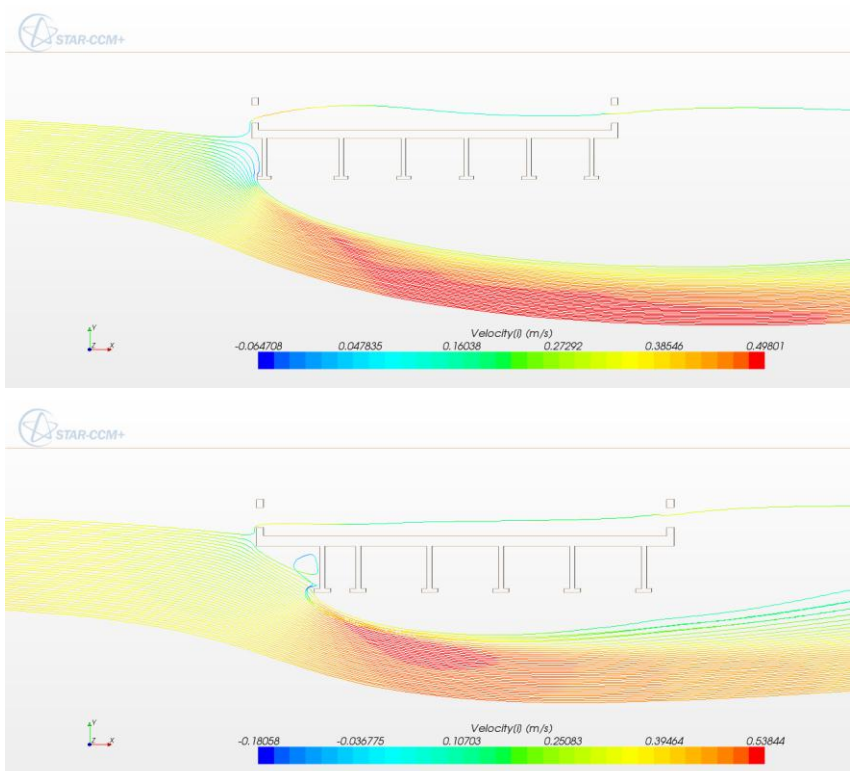

Figure 2.8: Numerical Simulation for Different Setbacks of 1st Girder

2.1.5. Dimensional Analysis Relations for Separation Zone Thickness

For the bottom-far-field condition, the following formula is developed:

$$\begin{cases} \dfrac{t}{h_t} = K_1 \left(\dfrac{1.1b\mu}{\rho\sqrt{g}}\right)^{n_1} \dfrac{1}{h_t^{2.5n_1}} & \text{if } h_u - h_b \geq b \\ \dfrac{t}{a} = K_2 \left(\dfrac{\mu}{\rho\sqrt{g}}\right)^{n_2} \dfrac{1}{a^{1.5n_2}} & \text{if } h_u - h_b < b \end{cases}$$

$$K_1 = c_1 e^{-\alpha}, K_2 = c_2 e^{-\alpha}$$

$$\alpha = l/b$$

Based on the numerical simulation in STARCCM+ using the standard bridge deck model with $\alpha_0 = l_0'/b = \frac{0.02}{0.029} = 0.69$, the coefficients above are determined as,

$$\begin{cases} K_1 = 408.3968, n_1 = 0.5184 & \text{if } h_u - h_b \geq b \\ K_2 = 1.0955, n_2 = -0.04717 & \text{if } h_u - h_b < b \end{cases}$$

For the shallow water condition, the following formula is developed:

$$\begin{cases} \dfrac{t}{h_t} = K_1 (Fr_t)^{n_1} \ (Re_t)^{m_1} \left(\dfrac{h_b}{h_u}\right)^{p_1} \left(\dfrac{h_t}{h_u}\right)^{q_1} & if\ h_u - h_b \geq b \\ \dfrac{t}{a} = K_2 (Fr_a)^{n_2} \ (Re_a)^{m_2} \left(\dfrac{h_b}{h_u}\right)^{p_2} \left(\dfrac{a}{h_u}\right)^{q_2} & if\ h_u - h_b < b \end{cases}$$

Fr_t is an effective Froude number defined as: $q_b/\sqrt{g}h_t^{3/2}$ for fully-submerged situation
Re_t is an effective Reynolds number defined as: $\rho q_b h_t/1.1b\mu$ for fully-submerged situation
h_t is the distance from water surface to bottom of bridge girders in fully-submerged situation
Fr_a is an effective Froude number defined as: $V/\sqrt{ga}$ for partially-submerged situation
Re_a is an effective Reynolds number defined as: $\rho Va/\mu$ for partially-submerged situation
a is the distance from water surface to bottom of bridge girders in partially-submerged situation
α is a geometrical factor defined as: l_o/b

The coefficients can be determined by correlating with existing experimental data sets. These relations may be modified to better fit the experimental data. Comparison of these relations with the trends of CFD predictions also needs to be done. Given that the Reynolds number for water flows is about 1 x 10^6 times the length and velocity scales, Reynolds numbers are expected to be well above 10,000, a low value that may be encountered at the laboratory scale, characteristic of fully turbulent flow. At high Reynolds numbers drag and associated separation and wake size tends to be at most only a weak function of Reynolds number. The Froude number for shallow water is a measure of flow speed divided by wave speed in free surface flows, and therefore the rate at which presence of downstream obstructions can be communicated upstream. Smaller Froude numbers are expected to correspond to conditions in which the flow has more time to react to and begin to turn around an obstruction, yielding a smaller turning angle and thinner separation zone around the side of the obstruction. Further

investigation is needed to determine if the relationship of these parameters to separation zone thickness is strong enough to include them in a correlation for the thickness.

2.1.6. Scale Up from Laboratory Scale to Full Size Bridge Deck

So far all the experiments and the simulations were conducted on the lab scale model which is about two orders of magnitude smaller than the typical real bridges. In the current quarter a comparative study was performed aiming to determine influence of the scale of the model on the results, i.e. on the separation bubble thickness underneath the inundated deck. For that purpose a model with a large domain around the bridge deck was built to simulate the deck acting as a bluff body in an infinite ocean. That way the influence of the boundaries and free water surface were eliminated. Three sizes of the domain and the deck were considered:

- A lab scale model (deck height of 0.058 m and domain of 2 m x 6 m)
- 10 times the lab scale model (deck height of 0.58 m and domain of 20 m x 60 m), and
- 100 times lab scale model (deck height of 5.8 m and domain of 200 m x 600 m)

In all models the number of cells was around 600,000. Different settings were used for the prism layer thickness to achieve reasonable accuracy of the results using wall functions to determine shear stress on the bridge deck wall boundaries. In all the models the water velocity was set to the lab experiment velocity of 0.4 m/s. The left domain boundary was set as a velocity inlet and the right one as a pressure outlet. The bed was modeled as a wall and all the rest of the boundaries were modeled as the symmetry planes.

The problems were calculated using the implicit unsteady solver. For each simulation different simulation time was set, based on selected time step of calculations. From the smallest model to the biggest the time steps used were 0.05 sec, 0.5 sec and 5 sec respectively. The corresponding simulation real time was 12 sec, 120 sec and 1200 sec respectively, approximately one domain residence time.

Figure 2.9: shows the velocity profiles in the three analyzed models. While they are similar for the lab scale model and 10x, the full scale 100x model has an unsteady wake using an unsteady k-epsilon turbulence model. Using a turbulent Reynolds number defined using the eddy viscosity, μ_t, in the wake region, this Reynolds number is around 35 for the 10x scale up and increases to near 500 for the 100x, full scale case. Under these conditions the mean flow in the RANS simulation becomes unstable and must be computed with using an unsteady RANS model. This unsteady behavior does not affect the separation zone thickness under the bridge deck, however. The ratio of separation zone thickness to deck height remains nearly constant from the laboratory scale to full scale.

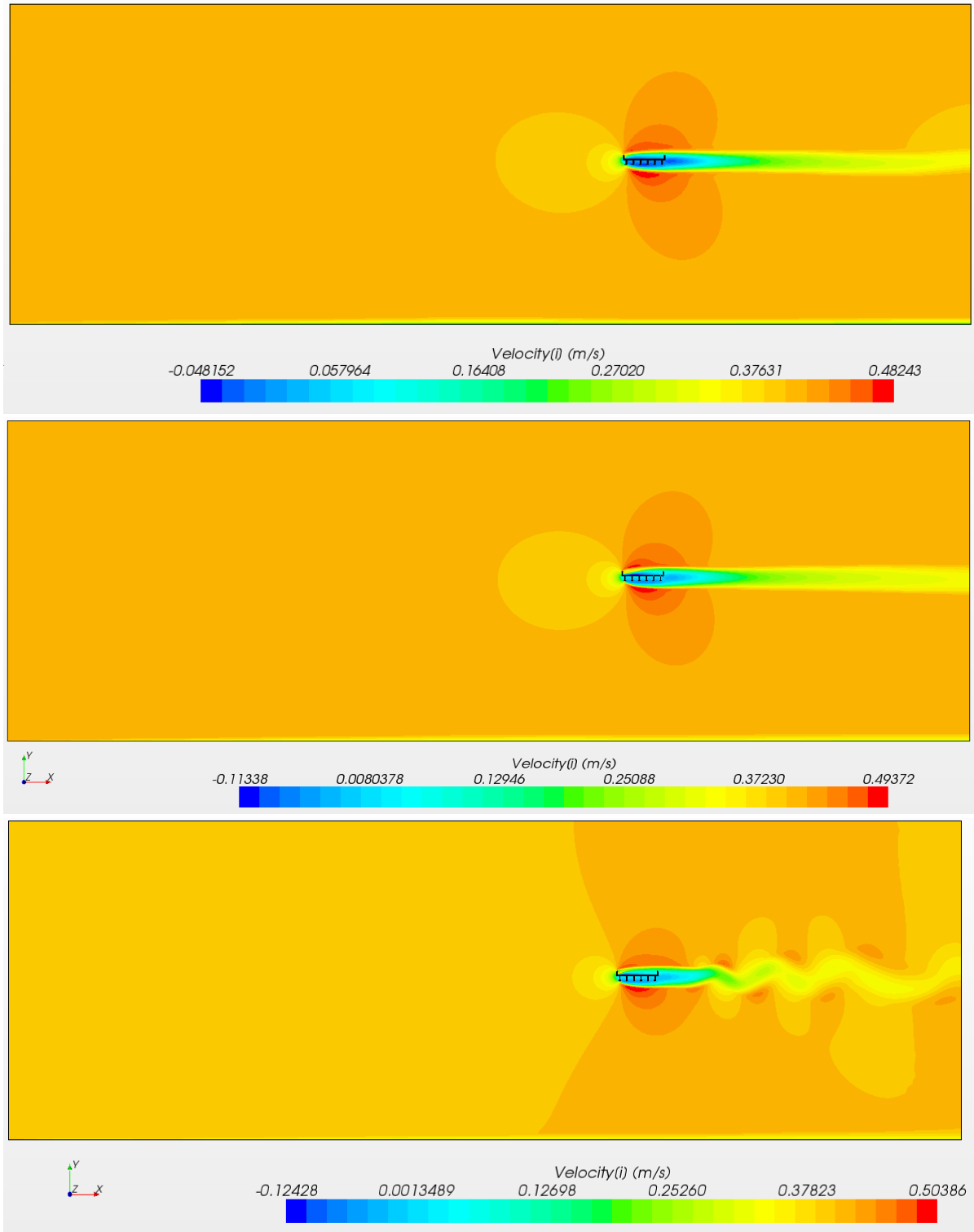

Figure 2.9: Velocity profile in the three models (top) lab scale (middle) 10 times the lab scale (bottom) 100 times the lab scale

Figure 2.10 shows the boundary streamlines for the separating flow. Based on these streamlines the thickness of the separation zones was determined.

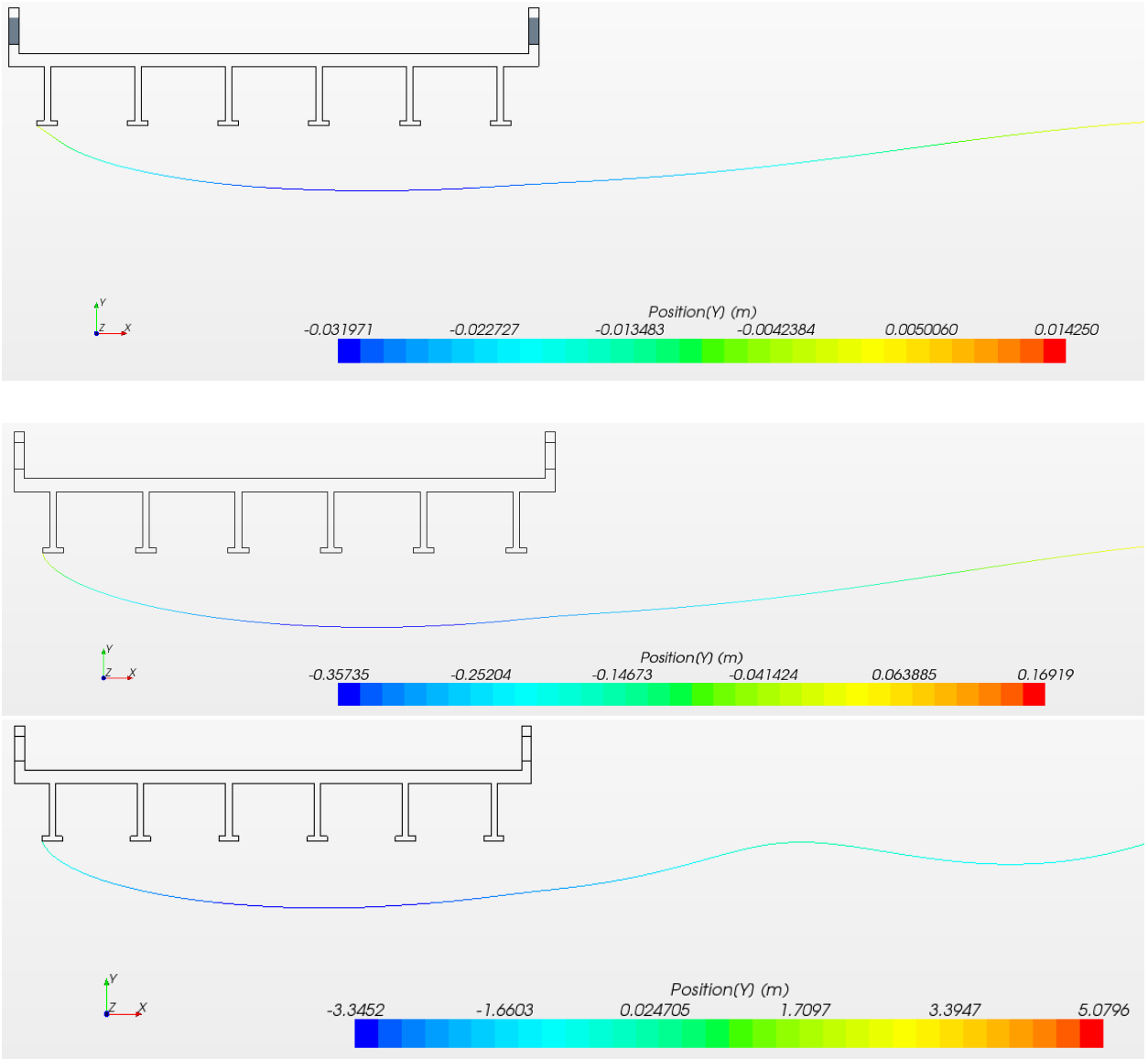

Figure 2.10: Boundary streamlines underneath the deck for three models

The thickness of the separation zone in these models was 0.0320 m in the lab scale model, 0.357 m in the 10 times bigger model and 3.34 m in the biggest model. These values are plotted in Figure 2.11 together with the ideal curve representing linear scaling of the thickness. The calculated results almost perfectly follow this ideal pattern. For this reason it can be concluded that the separation zone thickness is scaling linearly with the scale of the model and the lab scale results can be used to determine pressure scour conditions underneath the bridge. It has to be noted that this calculation was performed for the case where the river bed was far enough from the bridge deck so it was not influencing the results. However, when it is closer to the bed, the size of the sand grains need to be taken into account too as they are not linearly scaled with the size of the model and this linearity may be disturbed.

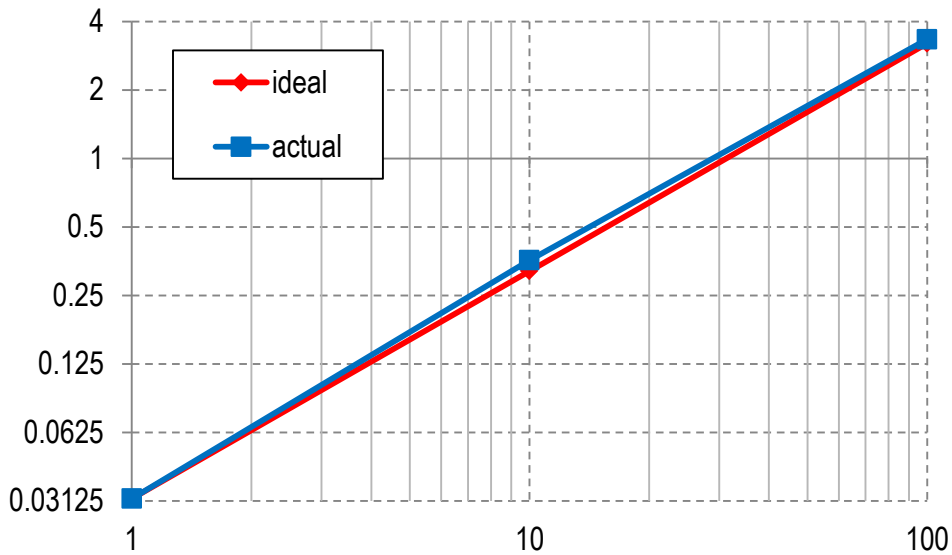

Figure 2.11: Thickness of the separation zone as a function of the scale of the model

2.2. Modeling of the Wind Tunnel Laboratory at TFHRC

2.2.1. Model Development

A study of the TFHRC wind tunnel CFD modeling was initiated in the previous quarter. The CFD model of the wind tunnel was created based on the CAD data provided by TFHRC. Multiple runs of the air flow through the tunnel in the laboratory room were conducted. In the initial runs the lab furniture was not included in the models. Also the method of modeling the screens in the tunnel as porous baffles was simplified. In the current quarter the most representative simulations out of the ones without the furniture were repeated with enhanced modeling of the screens. Also the model with the furniture in the lab room was created and analyzed. The current report documents the enhancements and the new results.

To replicate the screens installed in the tunnel a model of porous baffles was used. According to the STAR-CCM+ user guide [1] the pressure drop across a porous baffle can be modeled with the following equation:

$$\Delta p = -\rho(\alpha|v_n| + \beta)v_n \qquad 2.1$$

Where:

ρ - is the density of air,

v_n - is the normal velocity of air acting on the screen and

α and β are parameters that depend on screen geometry and properties.

In the literature only information about the possible derivations of α were found and the equation 2.1 was usually simplified to a form [2]:

$$\Delta p = -\frac{1}{2} K \rho {v_n}^2 \qquad 2.2$$

In the initial runs β parameter was assumed to be zero and α parameter was assumed to be constant (α = 0.3632). Setting parameter β to zero in Equation 2.1 we could relate α to the K parameter as:

$$K = 2\alpha \qquad 2.3$$

A more advanced formula by Weighardt defines *K* as a function of air normal velocity on the screens [3]:

$$K = 6.5 \left[\frac{1-\chi}{\chi^2}\right] \left[\frac{v_n d}{\chi v}\right]^{-\frac{1}{3}} \qquad 2.4$$

Where:

v_n - is the air velocity normal to the screens,

d - is the screen wire diameter and

ν - is the kinematic viscosity of the air.

Taking the diameter of the screen wire as 0.0075 inch, the kinematic viscosity of air as 15.68e-6 m/s^2 and normal velocity on the screens, the equation 2.4 was used to calculate α parameter each iteration using STAR-CCM+ field functions. The ideal definition would allow for taking into account a local value of the velocity on the screens. That would result in variable porous baffle parameters within a screen. However, this was not possible in the STAR-CCM+ and the velocity was taken as a surface averaged normal velocity of air. In Table 2.2 velocity measurements on the screens and calculated values of α for the model without the furniture are listed. The values for alpha are substantially different from the assumed initial value of 0.3632.

Table 2.2: Alpha parameter variation on the screens

screen number	normal velocity (m/s)	alpha (-)
1	8.532	0.442
2	8.498	0.442
3	6.516	0.483
4	4.937	0.530
5	3.803	0.578
6	2.892	0.634
7	2.118	0.703
8	1.847	0.736

2.2.2. Results

The first set of simulations model the system without the furniture in the room to determine the characteristics of the flow field in an empty room as a base case. In the initial model the mass flow through the fan inlet on the right side was 18.713 kg/s (15.54 m^3/s) and 17.058 kg/s (14.17 m^3/s) on the left side (The left side inlet is obstructed with a pulley plate for turning the fan). This reading was taken after 1000 iterations under steady state conditions. For each of the models additional 100 or more iterations were requested at the end of the simulation with updated values of alpha for each of the screens. At this stage the mass flows were read again. At the side obstructed with the pulley (pulley-side) the mass flow changed to 18.078 kg/s (15.27 m^3/s) and on the other side (no-pulley-side) the mass flow changed to 16.765 kg/s (14.16 m^3/s). Overall the change was about 2.6 %. This value is very small and can be said that is in the range of the uncertainty as the mass flow is oscillating (in third digit) during the simulation and is not converging to a greater extent when the number of iterations in increased.

Table 2.3 shows comparison of the mean air velocities registered between the screens and on the inlet and outlet of the extension of the tunnel for both initial and updated model. There is a drop in the mean velocity because of the increased resistance of the porous baffles. However, the change is very small and for each section is less than 3.0 %. This tendency was registered for all the other analyzed cases, so this comparison was not repeated in this report and only the final results are presented.

Table 2.3: Mean air velocity in the tunnel

location	initial model	updated model
section between 1st and 2nd screen	8.87	8.65
2 - 3	8.25	8.05
3 - 4	6.03	5.87
4 - 5	4.60	4.48
5 - 6	3.52	3.43
6 - 7	2.63	2.56
7 - 8	1.99	1.94
extension in	9.04	8.80
extension out	9.04	8.80

The model with the furniture was also updated. The cabinet was rotated and placed next to the tunnel's wall, as it is in the real lab. Figure 2.12 and Figure 2.13 show the velocity distribution in the lab in two cross sections – vertical and horizontal respectively. The horizontal cross section was created above the level of the computer desks so they are not visible in the figure. The higher elements of the furnishing are not influencing the returning flow to the fan inlets. 16.827 kg/s (14.21 m^3/s) of air is flowing through the obstructed fan inlet. 17.894 kg/s (15.11 m^3/s) of air is flowing through the other side of the fan. This is very close to the amount of air flowing through the fan in the model without the furniture in the room. The furniture is not negatively influencing the air mass flow in the lab.

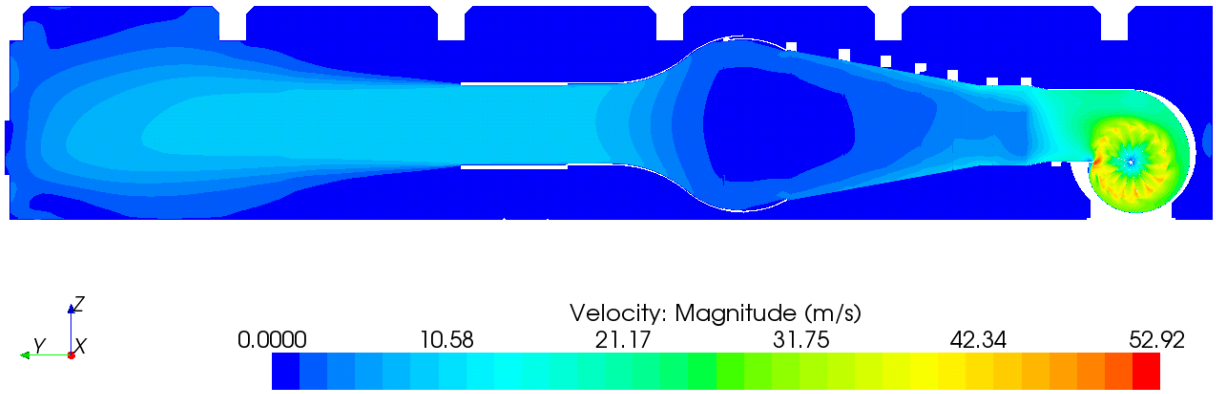

Figure 2.12: Velocity profile in model with the furniture – vertical plane

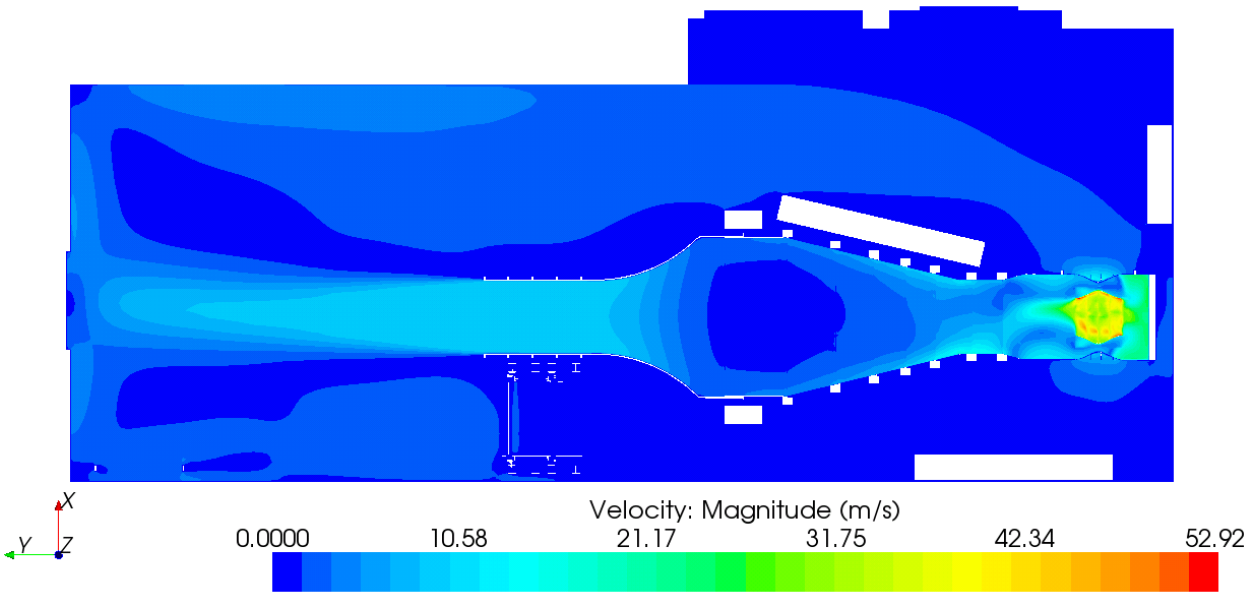

Figure 2.13: Velocity profile in model with the furniture– horizontal plane

Table 2.4 shows the surface averaged velocity of the air on the screens and corresponding to it the value of the alpha parameter. The values are not much different from the values in Table 2.2 for the model without the furniture.

TFHRC was interested in the quality of the flow inside of the tunnel extension and outside of it, approximately 4 to 5 ft downstream of the exit where tested objects are installed. For that purpose additional derived parts were created as vertical squares with the cross section size of the wind tunnel extension. In this report main focus was on the velocity distributions in the test sections, which are not in an enclosure, but out in the room.

Table 2.4: Alpha parameter variation on the screens

screen number	normal velocity (m/s)	alpha (-)
1	8.493	0.442
2	8.449	0.443
3	6.486	0.483
4	4.913	0.531
5	3.781	0.580
6	2.876	0.635
7	2.107	0.704
8	1.865	0.733

The following sections were considered:

- Outlet of the tunnel extension
- 2 ft beyond the outlet
- 3 ft beyond the outlet
- 4 ft beyond the outlet
- 5 ft beyond the outlet
- 6 ft beyond the outlet

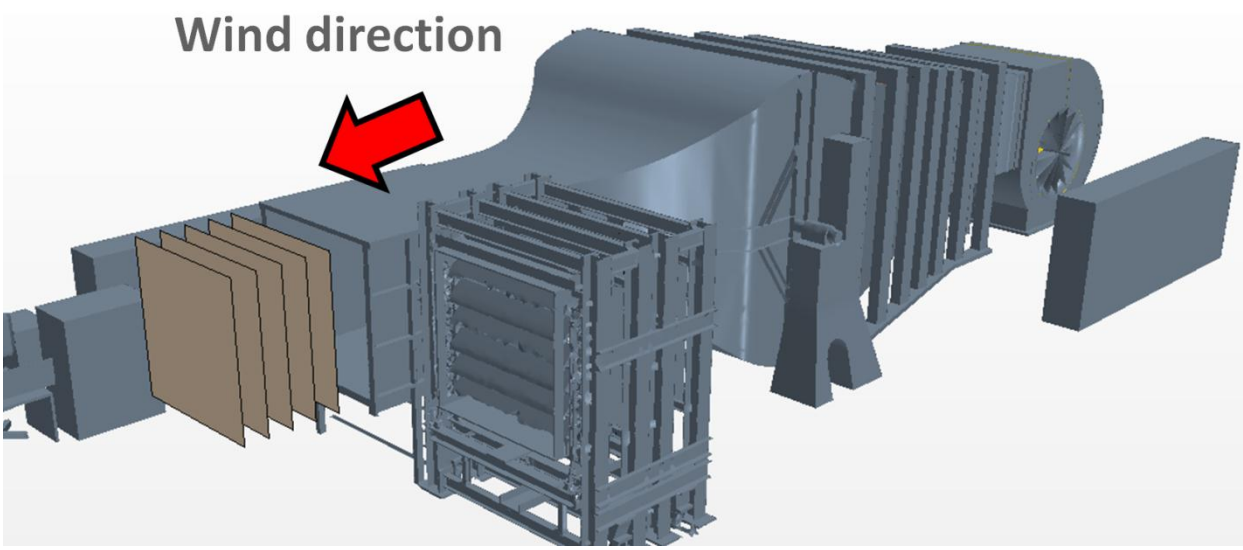

Figure 2.14: Location of the sections of interest in the model

When initial models and meshes were built and tested, the test section was assumed to be in the tunnel extension and a fine mesh in the internal flow region was judged to be sufficient. The mesh has now gone through several refinement tests for about 2 hydraulic diameters downstream of the tunnel exit for better assesment of the flow quality outside of the tunnel. As previously noted the room geometry and end wall have very little effect on the internal flow past the first couple of screens, but in an

external test zone, there are some room effects. The computational mesh around the testing section was significantly refined (cell size on the edges ~ 0.9 in). Figure 2.15 shows the new mesh outside of the tunnel extension in the testing section. The geometry of the pulley was not updated yet and it is still represented as a solid disc as it was in the CAD files. A recent meeting at the test facility revealed that the pulley is actually an open wheel with spokes, and that geometry will be incorporated into the model.

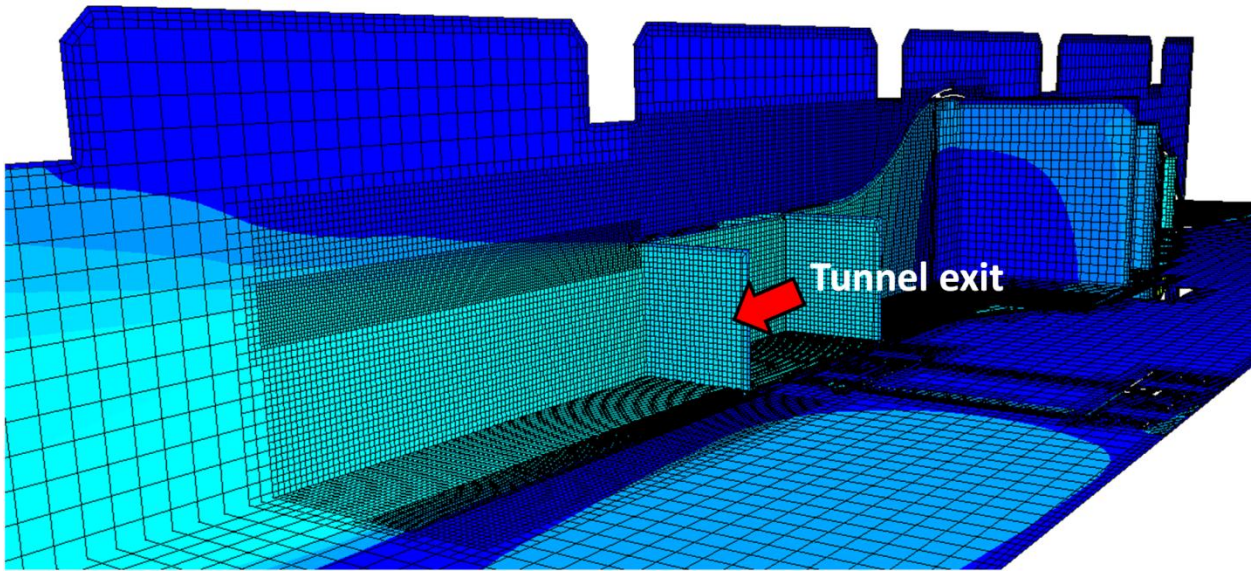

Figure 2.15: Mesh refinement outside of the tunnel extension

A literature search was performed on jet half angles. Based on G. Horn & M. W. Thring "Angle of Spread of Free Jets" Nature 178, 205 - 206 (28 July 1956) measured values of the jet half-angle have been variously reported from 7° to 20°. Using Prandtl's hypothesis, Tollmien calculated the jet half-angle to be 12°. An estimate based on our CFD analysis indicates that the angle is about 13.5° (influenced by the interaction with the end wall and where you draw the line for measurement). This value is in agreement with estimates form the literature.

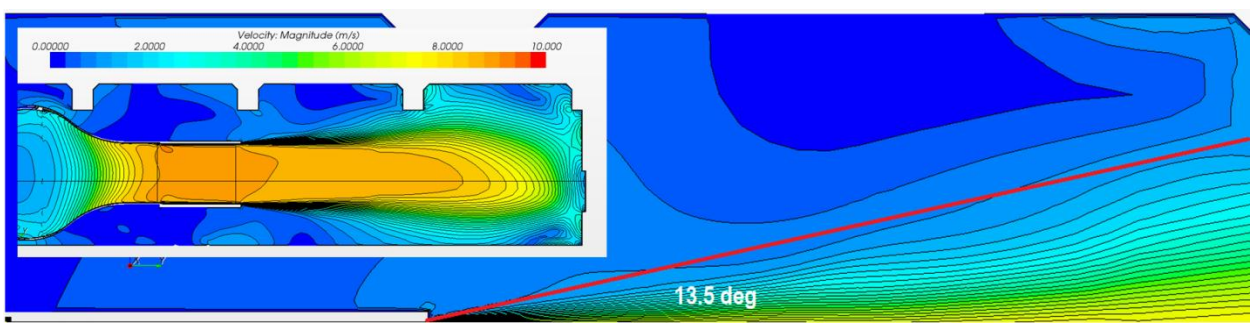

Figure 2.16: Measurement of the jet half-angle

The literature also indicates that the potential core (cone shaped for circular jets) will extend between 4 to 5 diameters downstream. The TFHRC test section is within one hydraulic diameter downstream of the tunnel exit, and the test bridges are close to the size of the exit opening width.

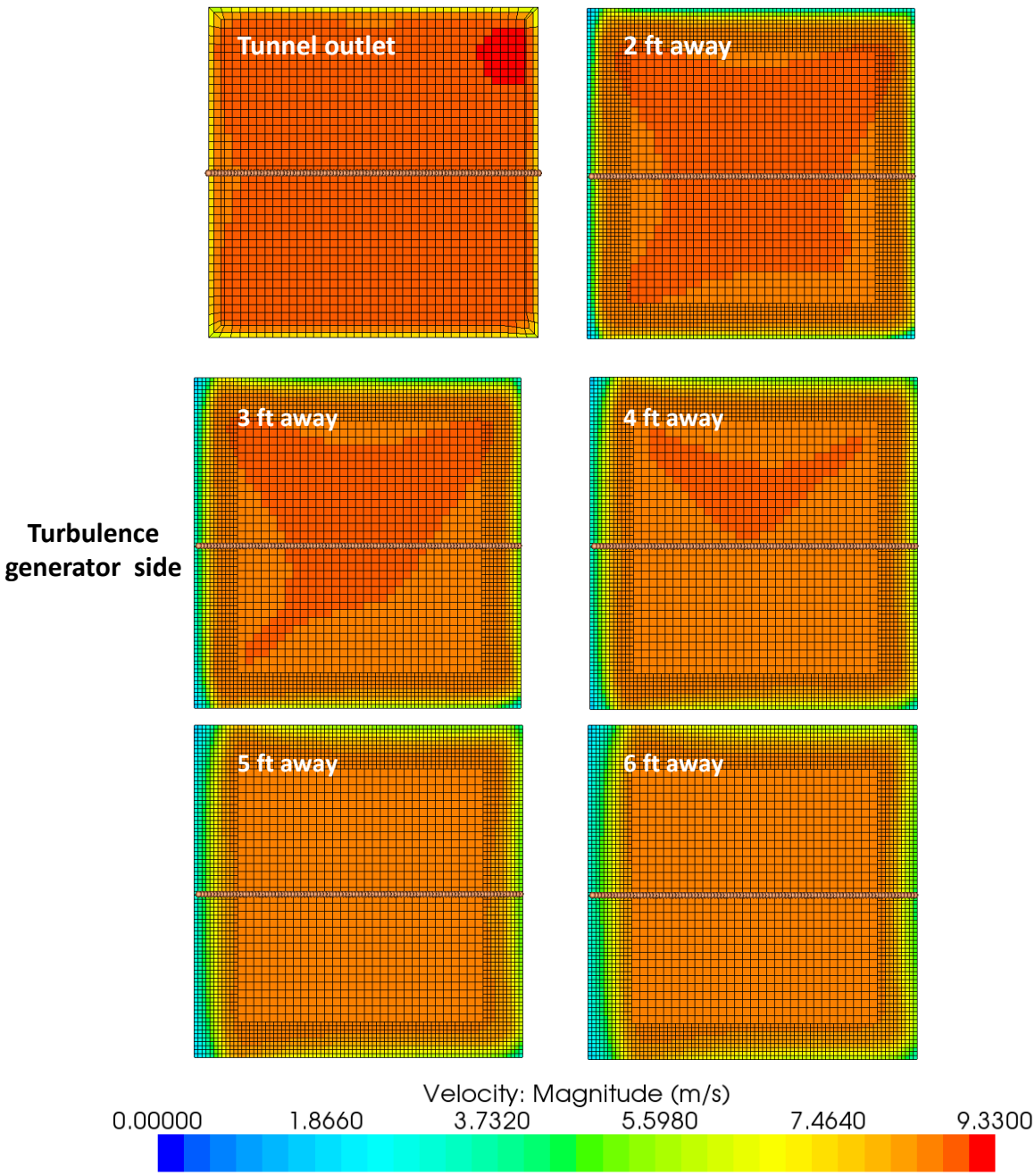

Figure 2.17: Velocity distribution in the section of interest

Figure 2.17 shows the velocity profiles in the testing sections. These profiles indicate that the velocity decreases more rapidly on the turbulence generator side of the jet than on the side with the larger amount of open space. Figure 2.19 present velocity distribution at the horizontal line running through the middle of the defined sections. The center of a 5 ft. bridge deck is shown aligned with the wind tunnel centerline. Asymmetries in room yield a smaller velocity drop on one side of the deck than the other. At 3 ft there is about 2 % drop in velocity at the ends. At 5 ft. downstream, a 8% drop on the turbulence generator side versus only a 4% velocity drop on the other side.

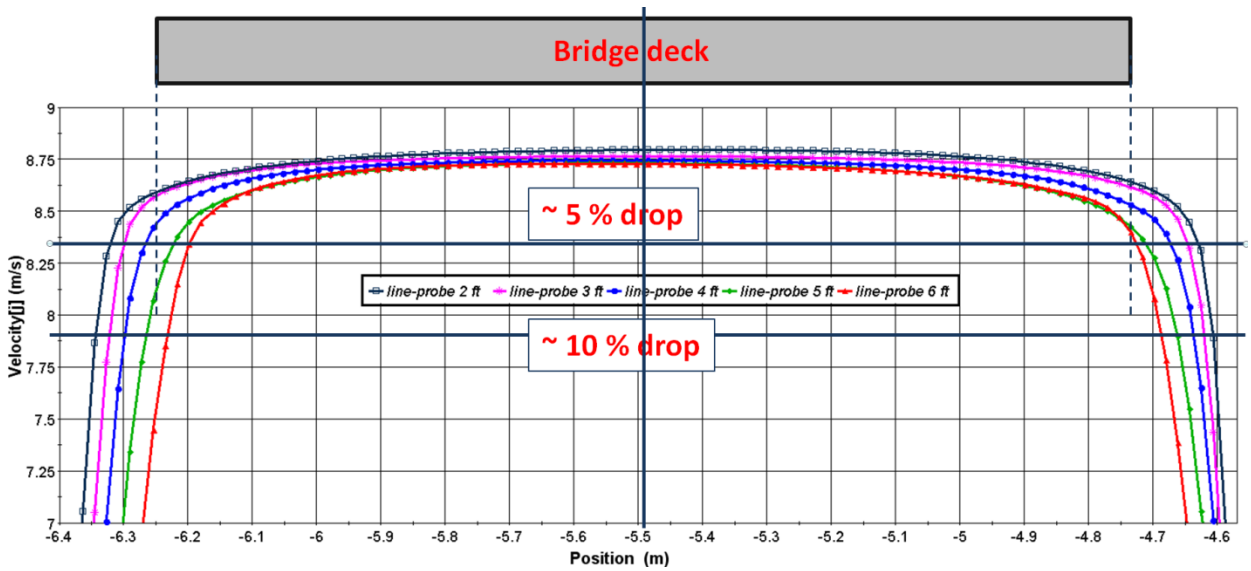

Figure 2.18: Velocity distribution downstream of the tunnel exit. Model with furniture, speed of fan 500 rpm.

Figure 2.19 presents a similar graph for the case where rotational velocity of the fan was dropped to 250 rpm from the initial value of 500 rpm. The velocity distribution in this case is more uniform on the edges of the bridge model. At 3 ft there is about 1 % drop in velocity at the ends. At 5 ft there is about 3 % drop on the turbulence generator side and about 1 % drop in velocity on the other side.

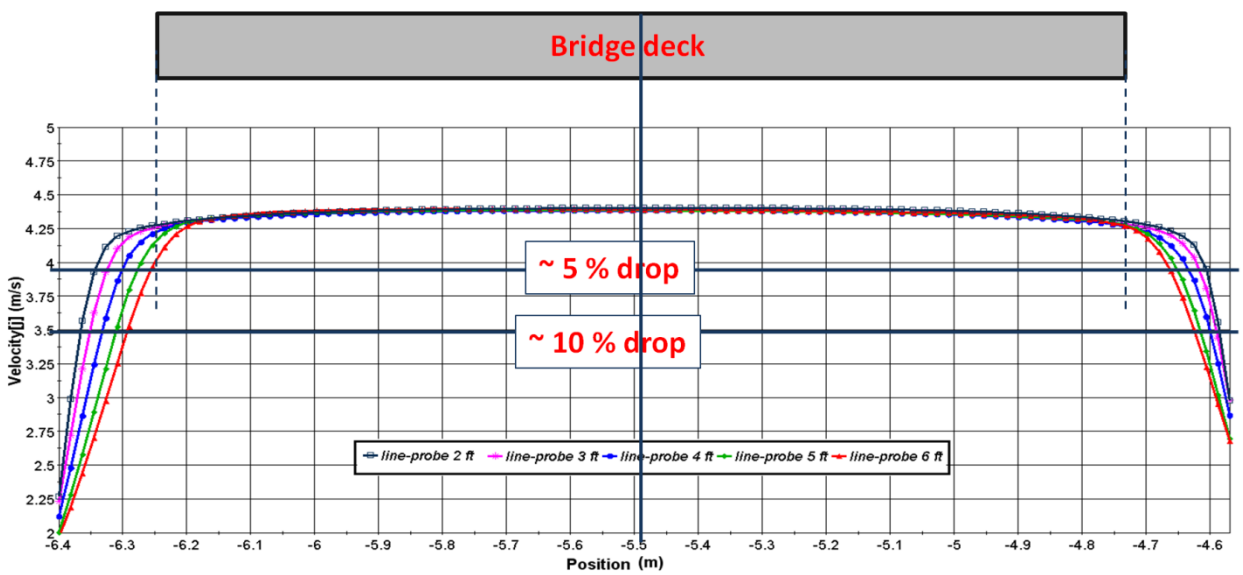

Figure 2.19: Velocity distribution downstream of the tunnel exit. Model with furniture speed of fan 250 rpm.

In this quarter the model with the installed turbulence generator was analyzed again. Figure 2.20 and Figure 2.21 show the velocity profiles in the room. Since the turbulence generator was not fully in its neutral position in the provided CAD files, the flow is not symmetrical and is also directed downward.

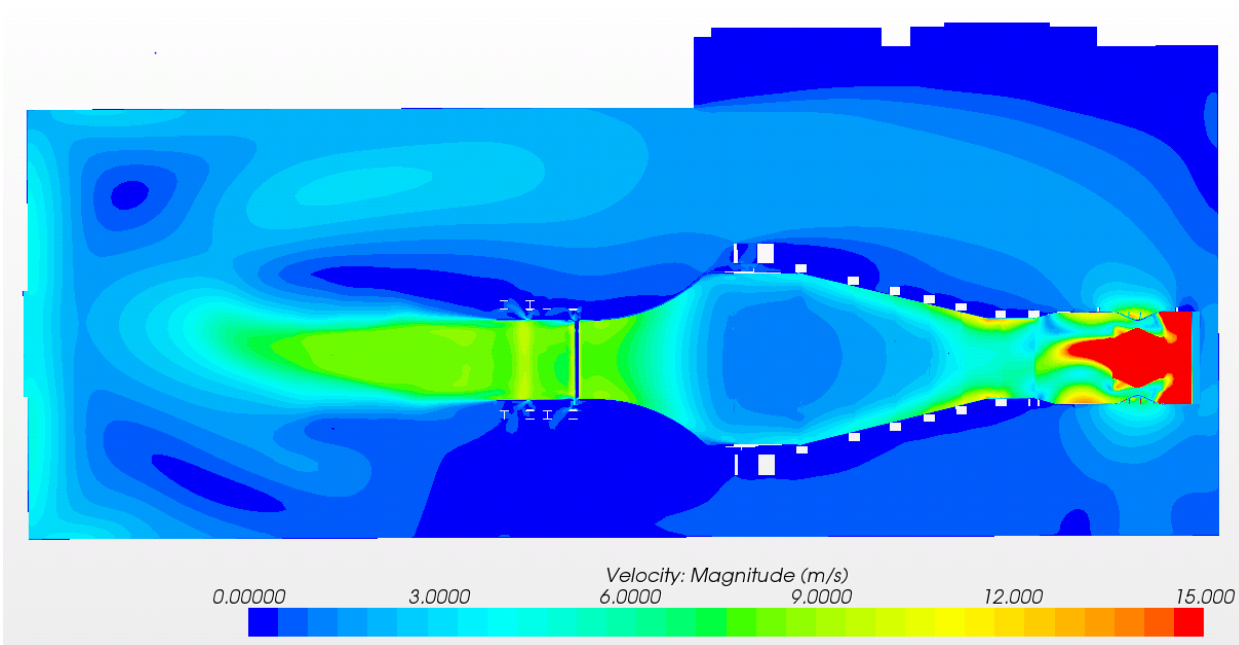

Figure 2.20: Velocity profile in model with the furniture – vertical plane

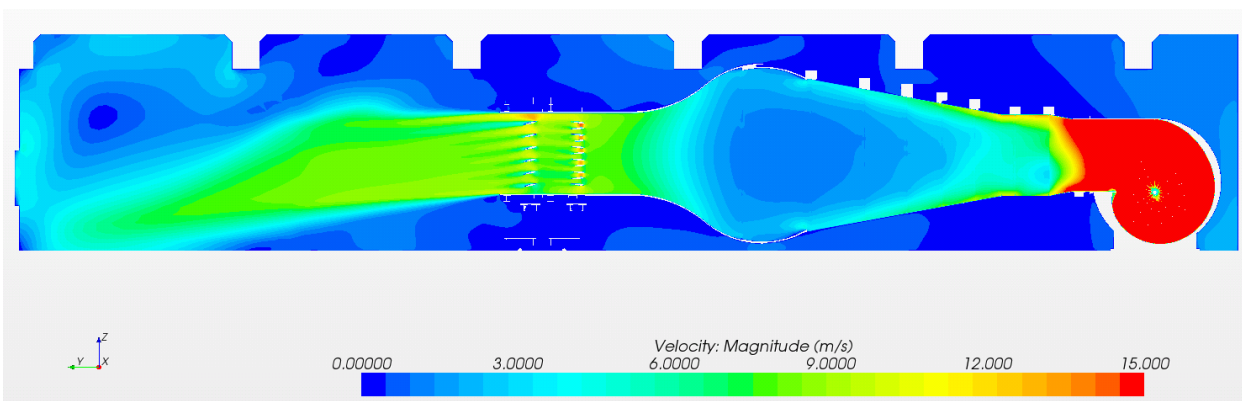

Figure 2.21: Velocity profile in model with the furniture – horizontal plane

This arrangement of vanes has a impact on uniformity of the flow in the testing section outside of the tunnel. Figure 2.22 shows velocity profiles in several cross sections outside of the tunnel. The further from the tunnel the more non uniform the flow is in the horizontal plane.

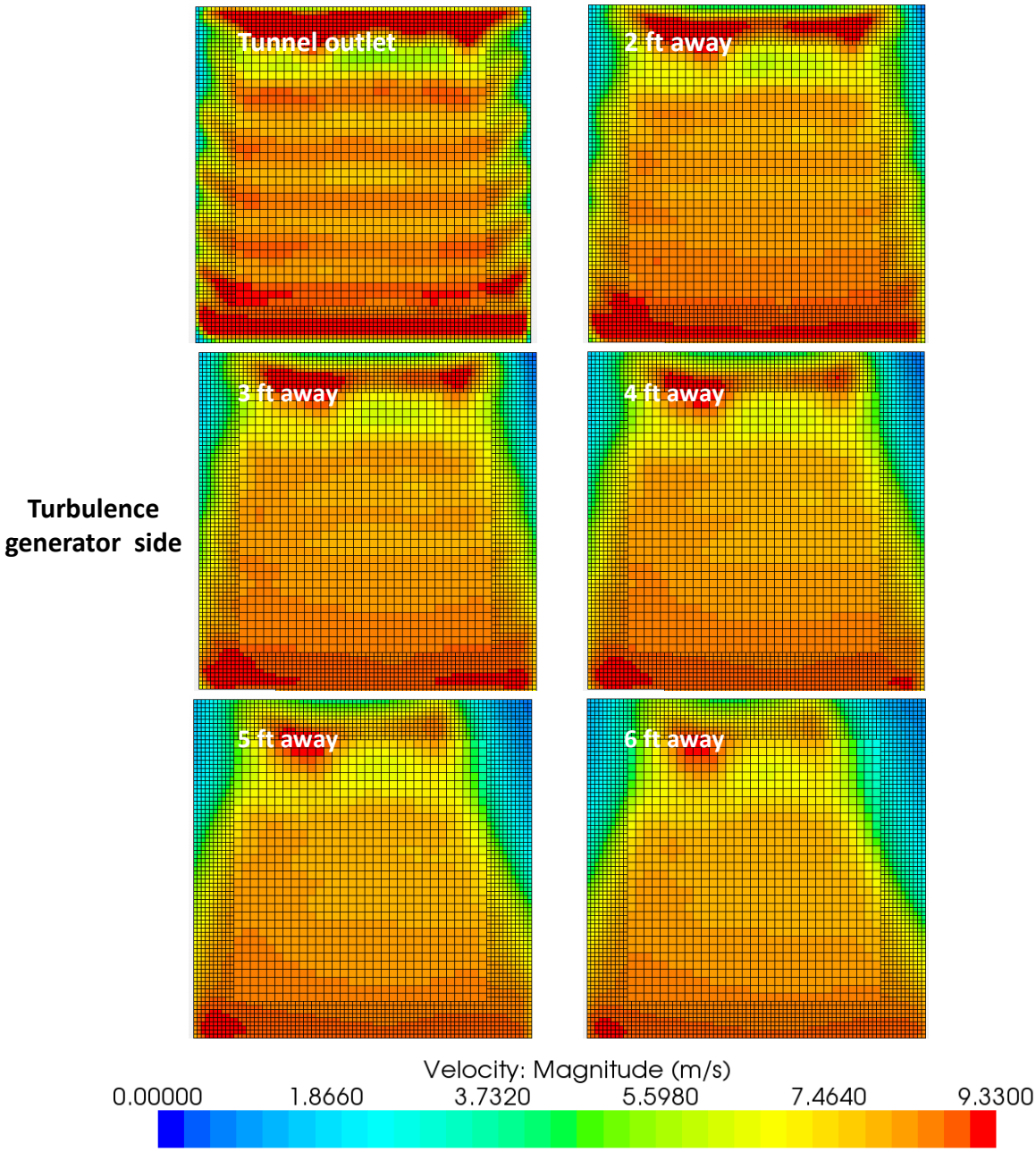

Figure 2.22: Velocity distribution in the section of interest

Figure 2.23 shows the velocity distribution at the horizontal line running through the middle of the defined sections with bridge deck aligned with the center of the wind tunnel. The plot shows a significant drop of the velocities on the edges of the testing section even for sections close to the outlet of the tunnel. Also the plot shows non-uniformity from left to right side of the room.

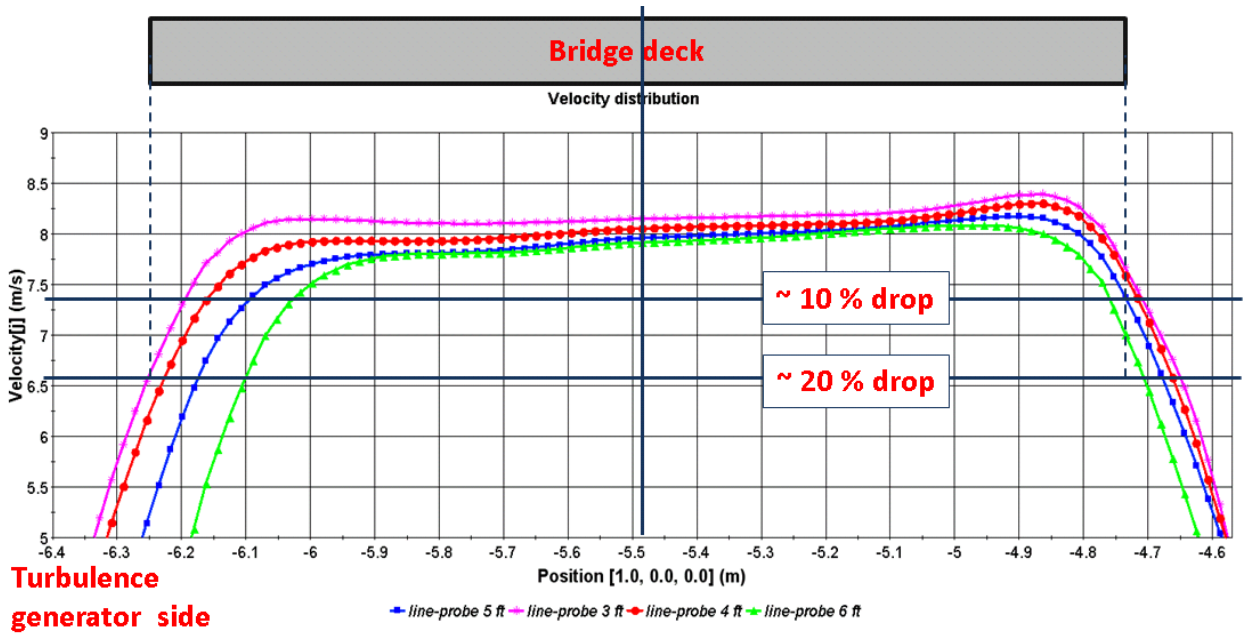

Figure 2.23: Velocity distribution downstream of the tunnel exit. Model with installed turbulence generator.

Further testing would be required to determine if there is a turbulence generator vane position that has only an acceptably small impact on the downstream flow pattern when the turbulence generator is not in active use.

2.2.3. References

[1] CD-adapco, *User Guide STAR-CCM+ Version 6.02.008*, 2011

[2] R.D. Mehta, *Turbulent Boundary Layer Perturbed by a Screen*, AIAA Journal, Vol. 2, No. 9, pp 1335-1342, September 1985

[3] R.D. Mehta, P. Bradshaw, *Design rules for small low speed wind tunnels*, The Aeronautical Journal of the Royal Aeronautical Society, November 1979

2.3. Modeling of the In-Situ Scour Testing Device

2.3.1. Model Development

TFHRC is working on the development of an in-situ scour testing device. The device is supposed to work as a propeller pointing directly toward the water bed. The stream of water generated by it will be eroding the bed and the rate of this erosion will be recorded. As an initial study a simple experiment was performed on a small plastic impeller rotating in the water above a sand covered bottom as shown in Figure 2.24 a. The propeller was rotating with the speed of 250 rotations per minute. After few seconds of the experiment the sand was eroded and a "scour hole" was created in the bed.

There was a question asked by TFHRC on shear stress distribution on the bed during this experiment. For that reason a CFD model was built that contained a domain for air, water and the propeller. The CAD data was provided by TFHRC. Initial velocity of the propeller was not provided so it was assumed to be 300 rpm. Also the size of the sand grains in the bed was unknown initially so it was assumed to be 1 mm. Further discussion revealed that the size of the sand grains in the real experiment was 0.5 mm so the model was updated accordingly.

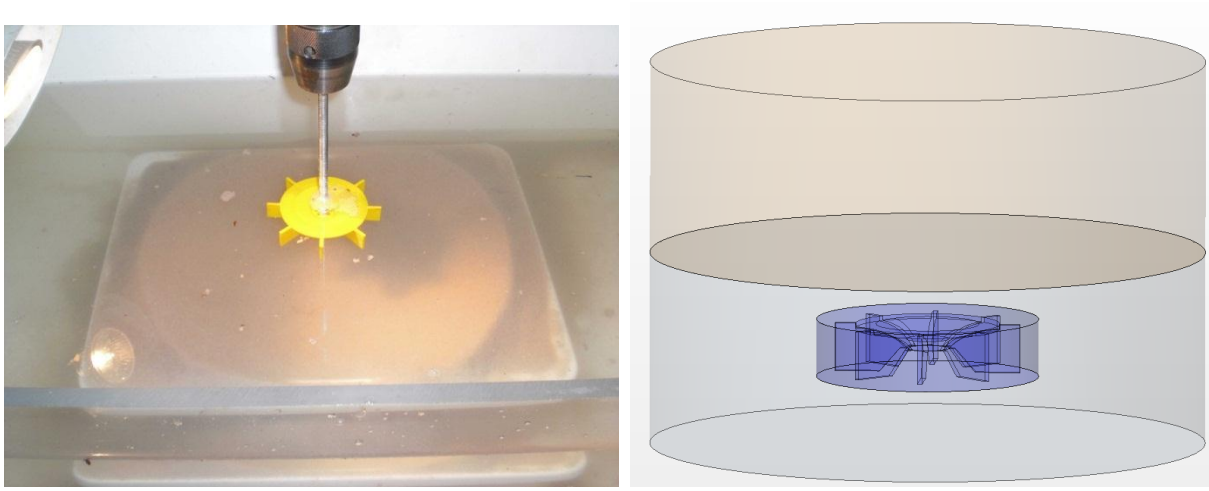

Figure 2.24: (a) The simple propeller experiment at TFHRC, (b) its CFD model

The CFD model presented in Figure 2.24 b was built of approximately 1,200,000 cells with very dense mesh around the blades to precisely capture complex geometry of the device. The model was complex not only due to the shape but also due to physics replicated in the simulation. An Eulerian multiphase model, the VOF model, for the multiphase mixture of water and air with surface reconstruction was used. A Lagrangian multiphase model was activated for tracking the sand particles. The rigid body motion solver was used to simulate rotation of the device. The implicit unsteady solver with 0.005 sec time step was used to solve the problem. 5.0 s of real time were simulated. Each time step consisted of 10 inner iterations which resulted in 10,000 iterations to compute 5.0 s of time.

2.3.2. Results

Figure 2.25 presents the reconstruction of the water surface at the end of the simulation. Figure 2.26 presents the distribution of the sheer stresses and the shear vectors on the lower boundary of the

domain respectively. The highest stresses are noticeable underneath the blades. In the center of the model the stresses are close to zero. The highest registered stress for this case was ~4.54 Pa.

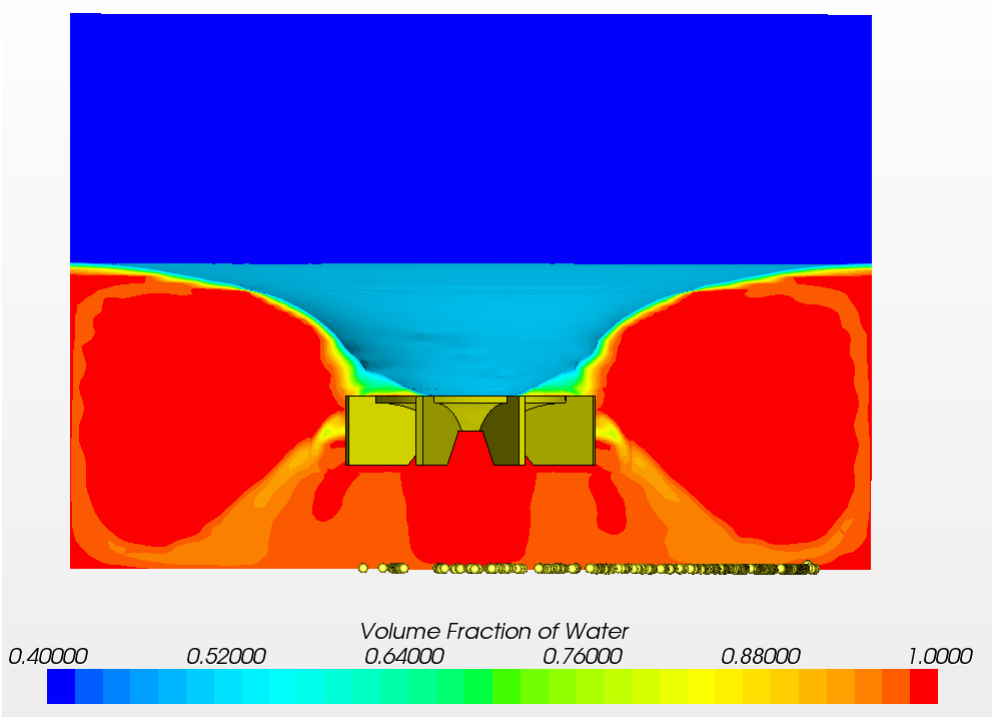

Figure 2.25: Reconstruction of the water surface in the simulation

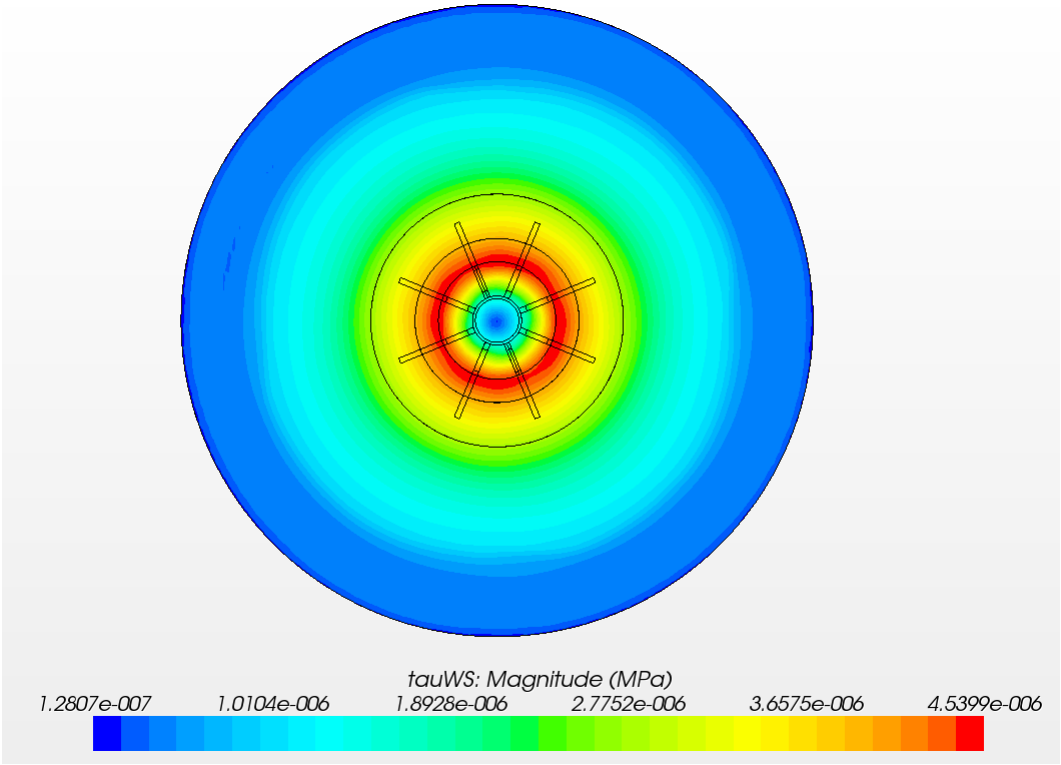

Figure 2.26: Shear stress on the bottom of the testing domain

In order to replicate the behavior of the sand bed, TRACC has worked on utilization of the Discrete Element Method (DEM) for representing individual sand grains. DEM has a big advantage over simple Lagrangian Particle tracking in dense particle flows in that it accounts for the interaction between the particles. However, it has turned out to be very cumbersome in implementation and cannot currently compute the flow of large numbers of particles (>~10^5) in a reasonable amount of computer time and therefore, for now this method was not pursued. In the coming quarters more tests will be conducted on it to see if it provides a good model for the upward transport of sediment via the auger of the in-situ device. In the current quarter Lagrangian Particle Tracking was used instead and only a small portion of the sand particles was simulated. A grid of injectors was located near the bottom surface of the model. Sand particles with 1 mm diameter were injected into the domain vertically upward with a small initial velocity of 0.005 m/s. The location of injectors is shown in Figure 2.27. The particles were injected at different stages of the simulation. At any time of the simulation the flow was not able to lift them much. The trajectories of particles are shown in Figure 2.28.

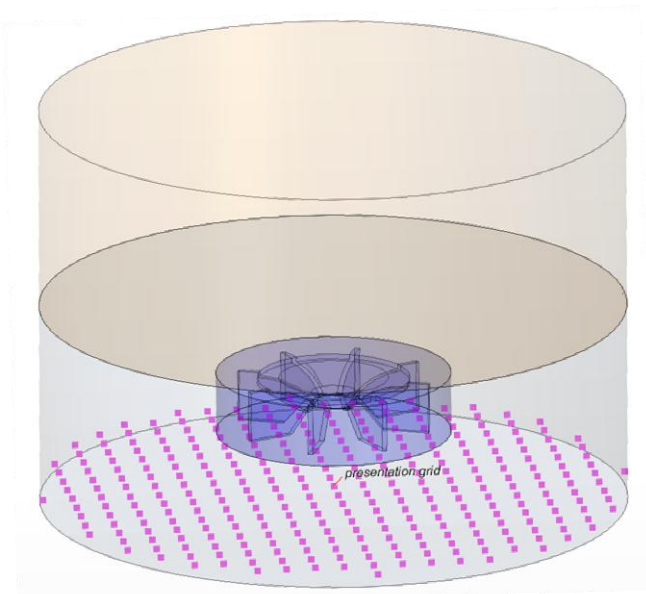

Figure 2.27: Location of the injectors of the particles

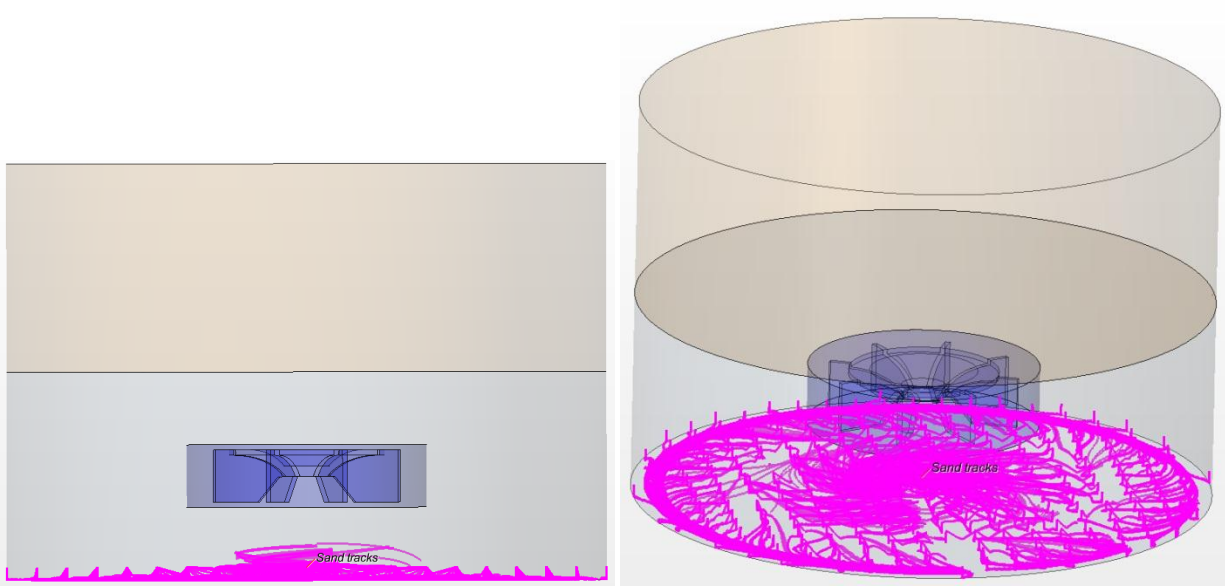

Figure 2.28 Trajectories of the 1 mm sand particles

As mentioned in the introduction the assumptions on the initial conditions were corrected by TFHRC once these initial results were presented. The actual angular velocity of propeller was changed from 300 to 250 rpm and sand particles with 0.5 mm diameter were injected instead of 1 mm. The water surface reconstructed in this simulation is shown in Figure 2.29.

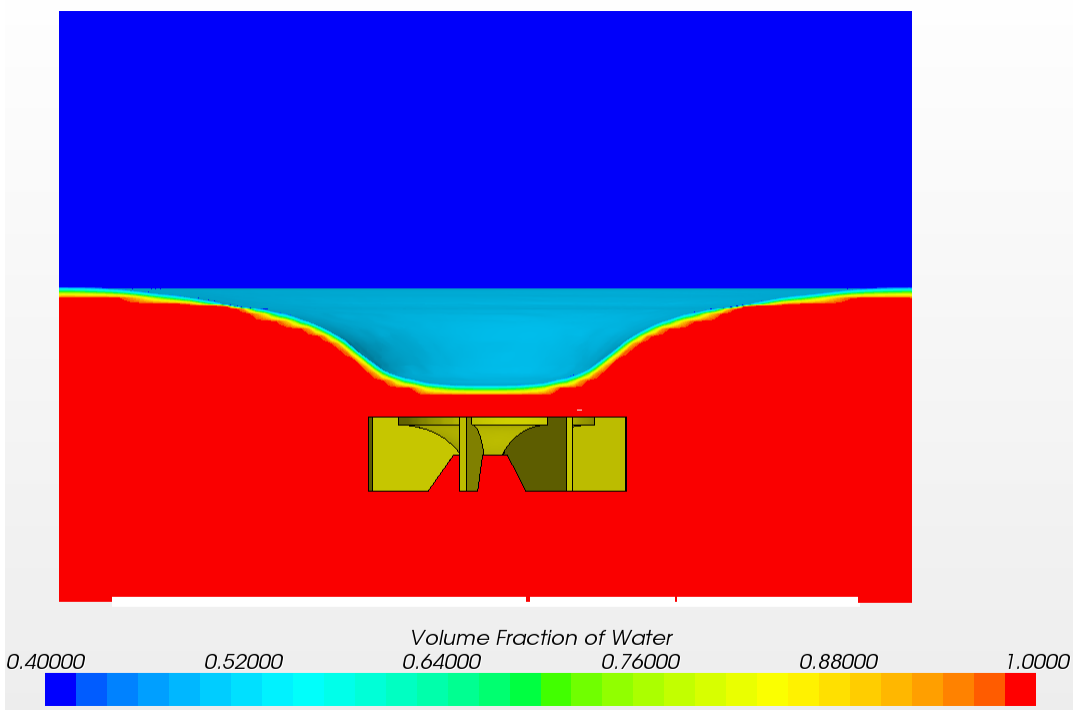

Figure 2.29 Reconstruction of the water surface in the updated model

The highest shear stresses dropped from 4.54 to 4.40 Pa in comparison to the initial simulation where the velocity of propeller was higher. The updated distribution of the shear stresses on the bed is shown in Figure 2.30.

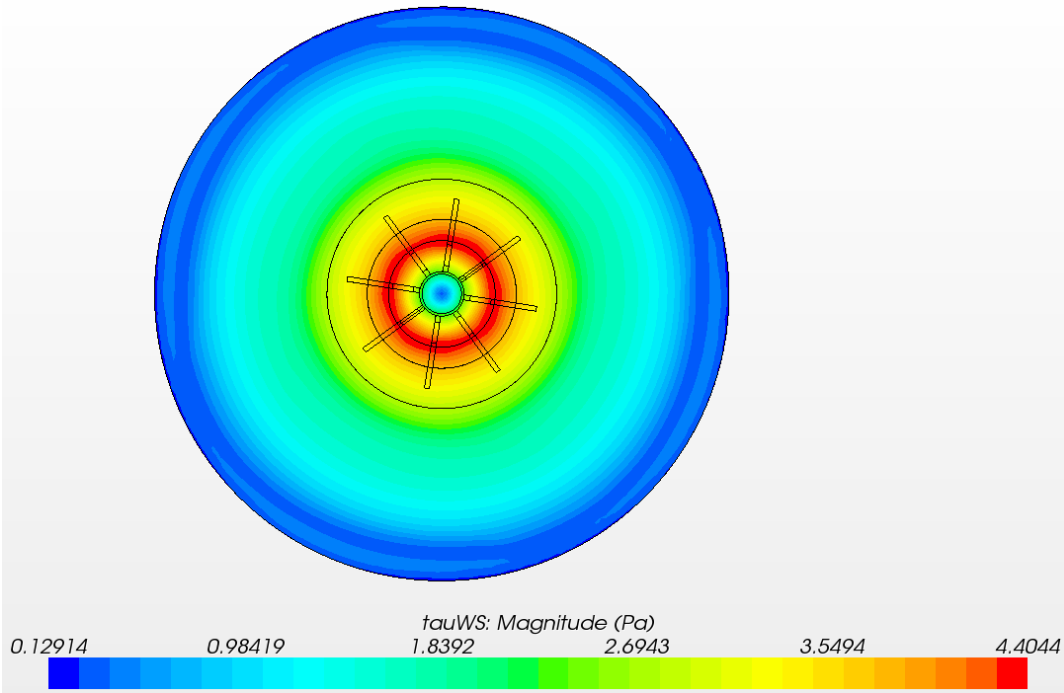

Figure 2.30 Real shear stress distribution on the bottom

Although the particles injected this time were two times smaller in diameter than previously, they were not raised much from the bottom either. Their trajectories are shown in Figure 2.31. Almost all particles ended up on the ground moved close to the external boundary of the domain where the shear stress was near zero. The final location of the particles is shown in Figure 2.32.

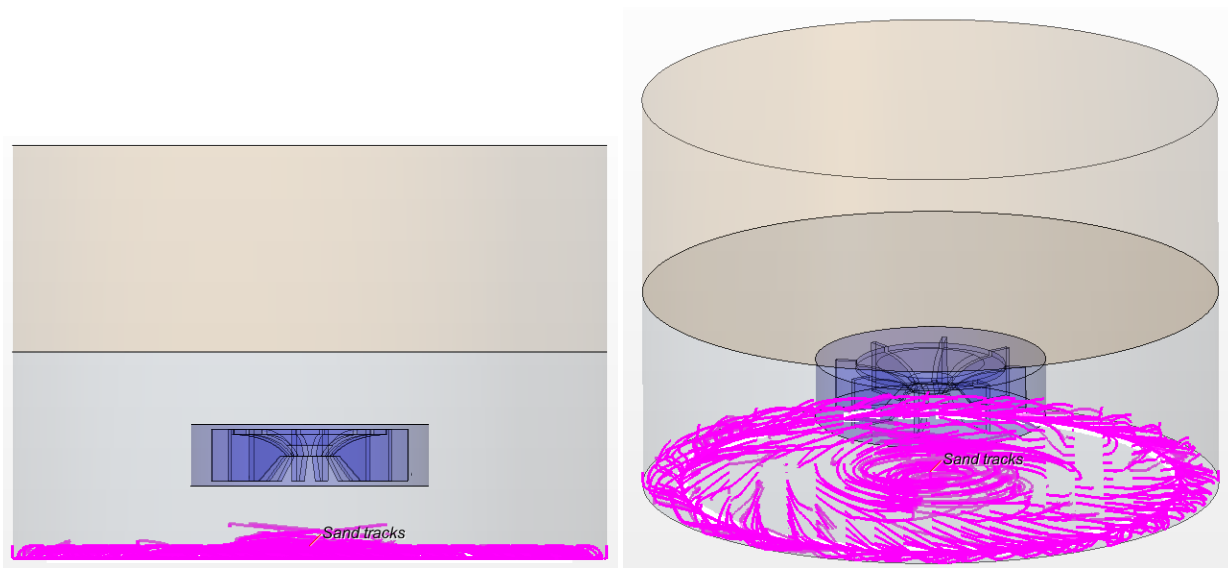

Figure 2.31 Trajectories of the sand particles

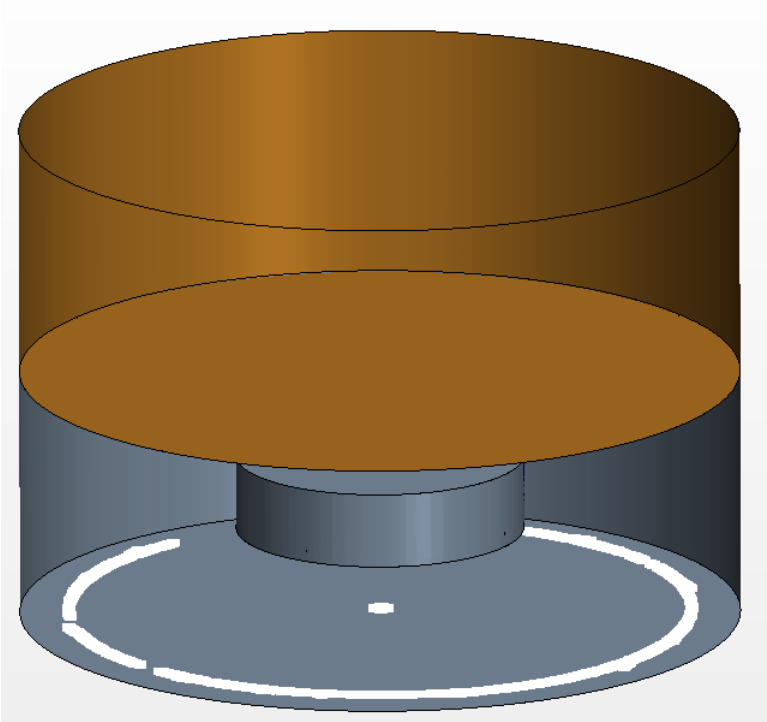

Figure 2.32 Final location of the sand particles shown in white

2.4. Computational Modeling and Analysis of Flow through Large Culverts for Fish Passage

Fish passage through culverts is an important component of road and stream crossing design. As water runoff volume increases, the flow often actively degrades waterways at culverts and may interrupt natural fish migration. Culverts are fixed structures that do not change with changing streams and may instead become barriers to fish movement. The most common physical characteristics that create barriers to fish passage include excessive water velocity, insufficient water depth, large outlet drop heights, turbulence within the culvert, and accumulation of sediment and debris. Major hydraulic criteria influencing fish passage are: flow rates during fish migration periods, fish species, roughness, and the length and slope of the culvert.

The objective of this work is to develop approaches to CFD modeling of culvert flows and to use the models to perform analysis to assess flow regions for fish passage under a variety of flow conditions. The flow conditions to be tested with CFD analysis are defined in the tables of a work plan from TFHRC [6]. The CFD models are being verified by comparing computational results with data from experiments conducted at TFHRC. A primary goal of CFD analysis of culverts for fish passage is to determine the local cross section velocities and flow distributions in corrugated culverts under varying flow conditions. In order to evaluate the ability of fish to traverse corrugated culverts, the local average velocity in vertical strips from the region adjacent to the culvert wall out to the centerline under low flow conditions will be determined.

A primary goal of the CFD analysis during this quarter has been to investigate methods to model gravel in the culvert. The test matrix in the TFHRC work plan [6] includes tests with the bed height at 15% and 30% of the culvert diameter. For these cases, the culvert bed material is coarse gravel with a mean diameter, D_{50} = 12 mm. At this gravel size, the gravel bed boundary cannot be treated as a rough wall using wall functions because the centroid of the near wall computational cell must be at a position that is greater than the roughness height. For 12 mm gravel, the near wall mesh would be far too large for the analysis results to be mesh independent. Two options to model flow parallel to a porous gravel bed are (1) to treat the bed as a porous media, with a flat interface dividing the two flow zones, and (2) to mesh out the rough bed contour created by the top layer of gravel. The methods for generating various velocity averages over a cross section from the work plan [6] that may be applied in improved fish passage analysis are summarized in section 2.4.1, and comparisons with experiments are also shown in the figures.

2.4.1. Modeling Culvert Flow above a Gravel Bed

A primary goal of the CFD analysis during this quarter has been to investigate methods to model gravel bed in the culvert. The test matrix in the TFHRC work plan includes tests with the bed height at 15% and 30% of the culvert diameter. For these cases, the culvert bed material is coarse gravel with a mean diameter, D_{50} = 12 mm. Since the experiments in the TFHRC were conducted by gluing a layer of gravel on the flume bed, meshing out the rough bed contour created by the top layer of gravel is a method to calibrate CFD modeling the culvert flow above a gravel bed.

2.4.1.1. Tests scenarios

During this quarter, both experiments and CFD model simulated the bed elevation for 0.15 culvert diameter situations. The flow velocities are 0.71 ft/s and 1.1 ft/s, and the water depths are 4.5 inch, 6 inch, and 9 inch. The specified proposal gravel with a mean diameter, D_{50} = 12 mm, which was used in the CFD model, while in the real experiments we used D_{50} = 10.5 mm. The sketch of the flume with the corrugated pipe is shown in Figure 2.33.

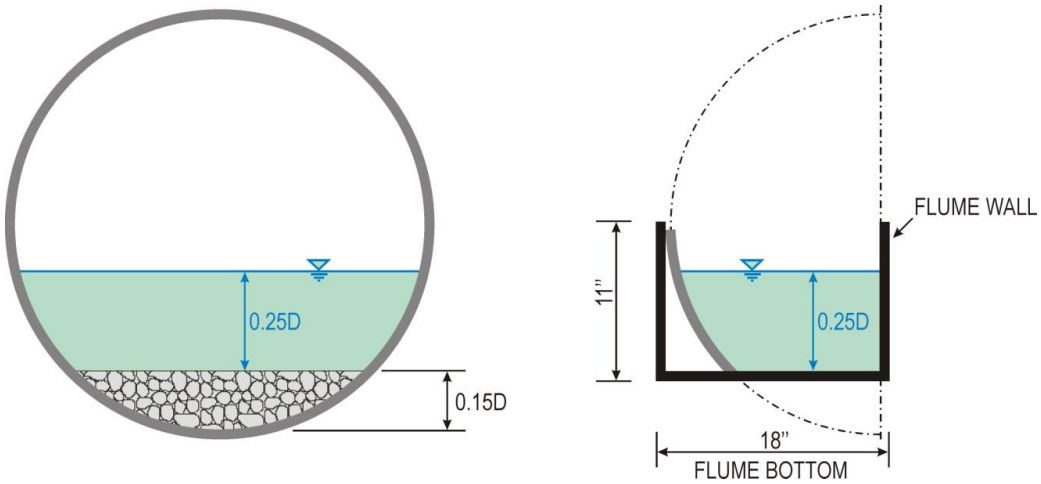

Figure 2.33: Bed elevation at 0.15 culvert diameter and symmetrical half of flume culvert model

2.4.1.2. CFD modeling methodology

Briefly, the method of mimicking the gravel in the CFD model is to mesh out the rough bed created by a half layer of gravel. The CAD model was created in Pro-ENGINEER. Figure 2.34 illustrates the method of creating a D_{50} =24mm gravel. In order to avoid the numerical error caused by sharp angles between grids, two quarter-circular arcs with the diameter of D_{50} are used to get smooth connections. Then the curve is rotated around the axis to create a flume bed surface bump approximation of a piece of gravel, and these are replicated over the flume bed model to create a rough bed with large roughness elements on the flume bed. Figure 2.35 shows the truncated model with the bed surface created by the gravel geometry.

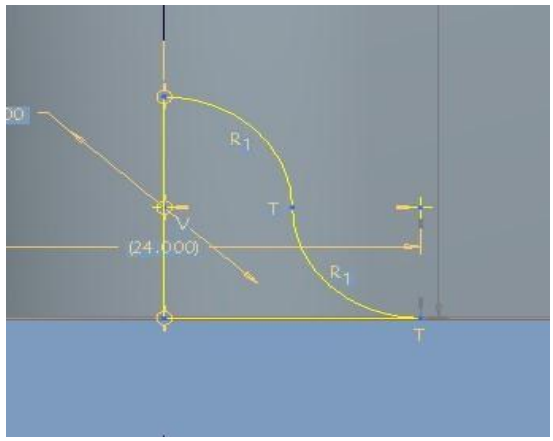

Figure 2.34: Illustration of the gravel creation method in the CAD model

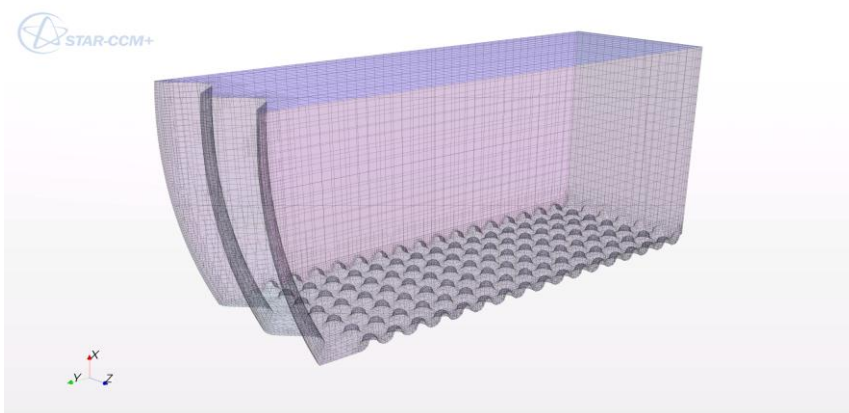

Figure 2.35: Truncated CAD model with the culvert bed surface created by the model gravel geometry

2.4.1.3. Comparison between CFD and experimental results

In order to calibrate the CFD model with the experimental results, the velocity distribution and magnitude between the CFD and PIV, the CFD and ADV is compared in corresponding areas. All the figures are derived from uniform data, which were interpolated once from the original computational cell data and observed data. The depth-averaged velocity and cumulative average velocity curves are developed based on the CFD data. The comparisons between CFD and experimental results and the velocity curves developed under different flow conditions are illustrated in Figure 2.36 through Figure 2.47.

1) Velocity is 0.71 ft/s, and the water depth is 4.5 inch

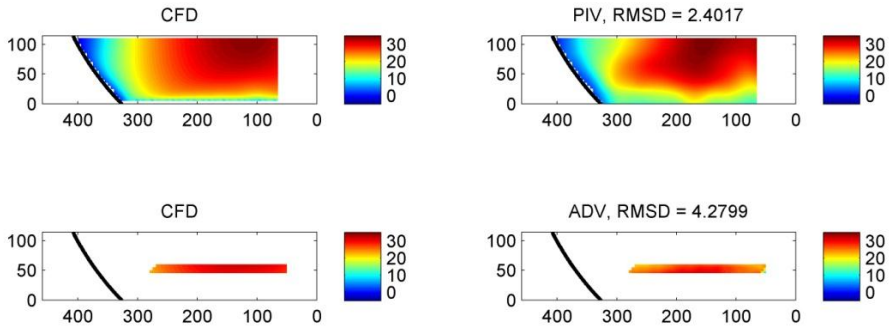

Figure 2.36: Comparison of the velocity distribution contour between CFD and PIV, CFD and ADV under the flow condition of 0.71fts and 4.5inch water depth

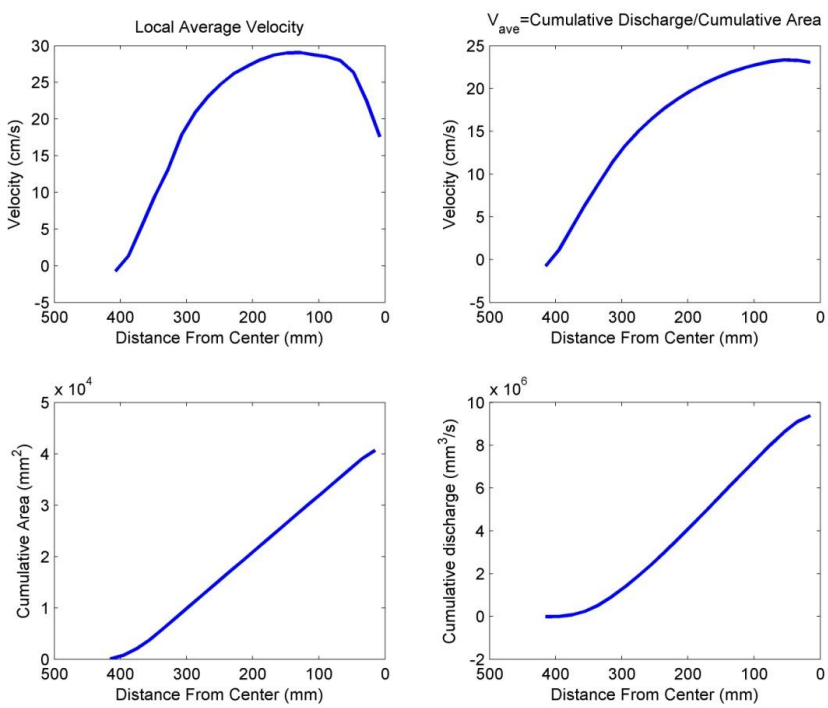

Figure 2.37: Depth-averaged velocity and cumulative average velocity curves development under the flow condition of 0.71fts and 4.5inch water depth

2) Velocity is 0.71 ft/s, and the water depth is 6 inch

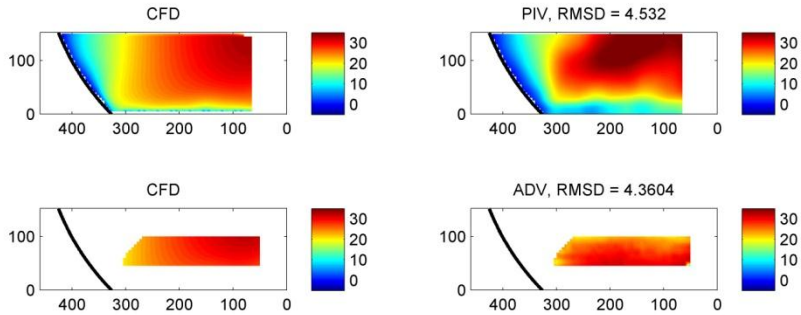

Figure 2.38: Comparison of the velocity distribution contour between CFD and PIV, CFD and ADV under the flow condition of 0.71fts and 6 inch water depth

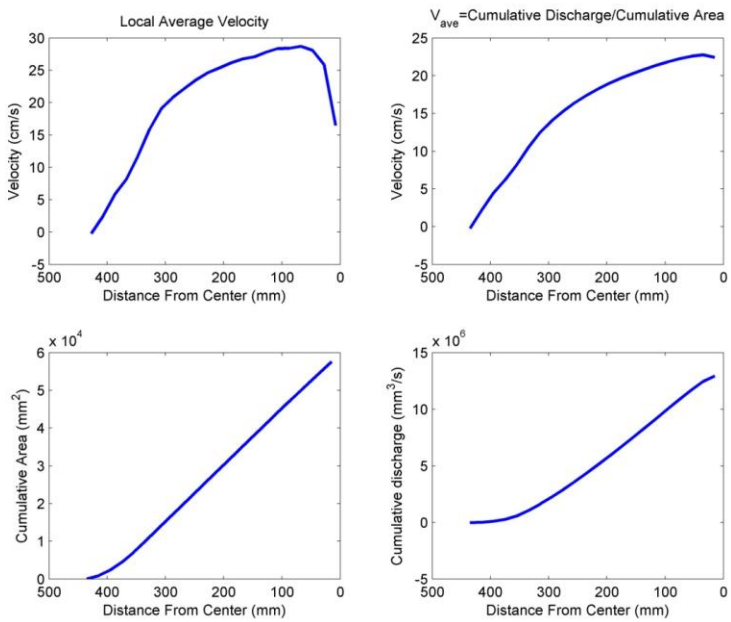

Figure 2.39: Depth-averaged velocity and cumulative average velocity curves development under the flow condition of 0.71fts and 6 inch water depth

3) Velocity is 0.71 ft/s, and the water depth is 9 inch

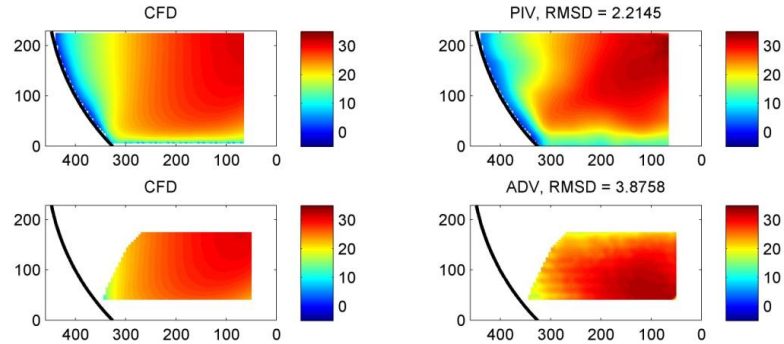

Figure 2.40: Comparison of the velocity distribution contour between CFD and PIV, CFD and ADV under the flow condition of 0.71fts and 9 inch water depth

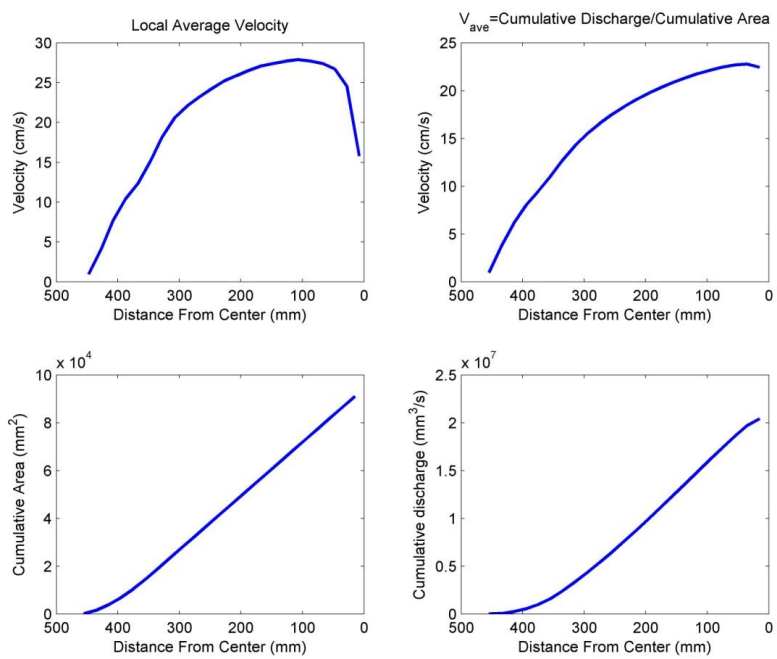

Figure 2.41: Depth-averaged velocity and cumulative average velocity curves development under the flow condition of 0.71fts and 9 inch water depth

4) Velocity is 1.1 ft/s, and the water depth is 4.5 inch

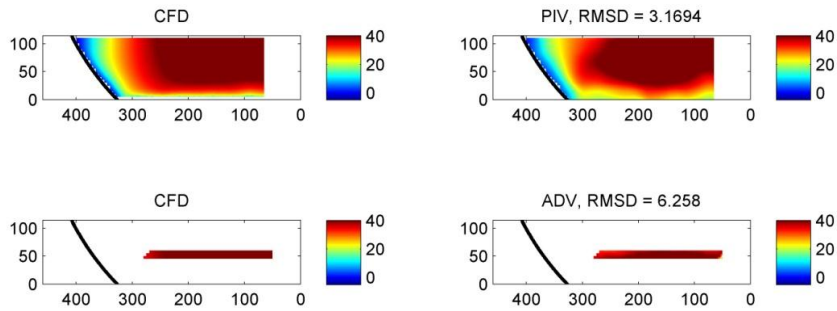

Figure 2.42: Comparison of the velocity distribution contour between CFD and PIV, CFD and ADV under the flow condition of 1.1fts and 4.5 inch water depth

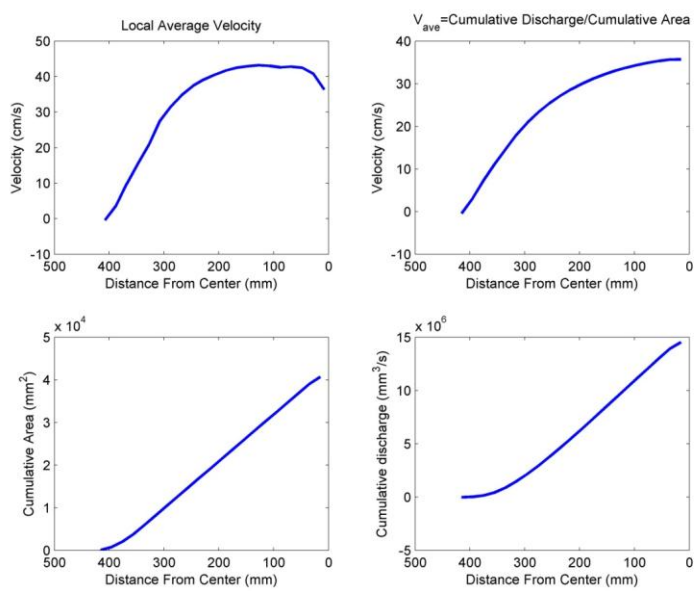

Figure 2.43: Depth-averaged velocity and cumulative average velocity curves development under the flow condition of 1.1fts and 4.5 inch water depth

5) Velocity is 1.1 ft/s, and the water depth is 6 inch

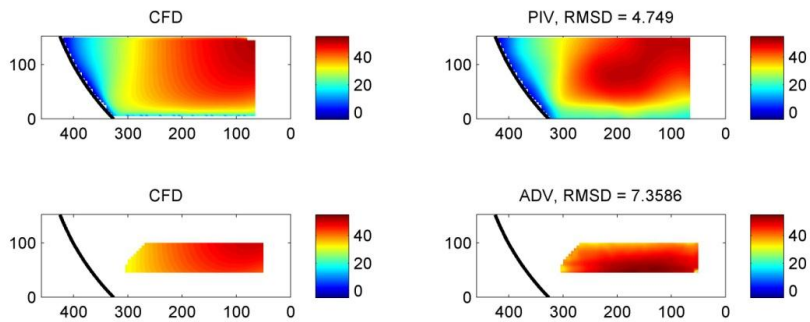

Figure 2.44: Comparison of the velocity distribution contour between CFD and PIV, CFD and ADV under the flow condition of 1.1fts and 6 inch water depth

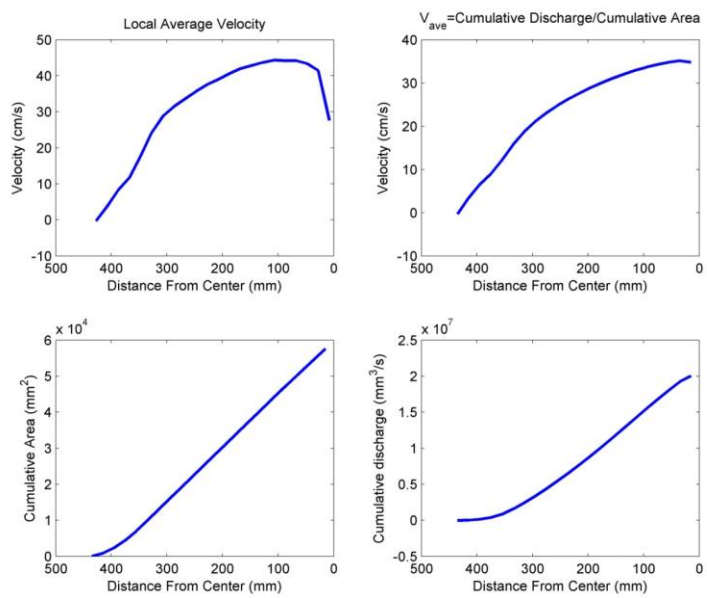

Figure 2.45: Depth-averaged velocity and cumulative average velocity curves development under the flow condition of 1.1fts and 6 inch water depth

6) Velocity is 1.1 ft/s, and the water depth is 9 inch

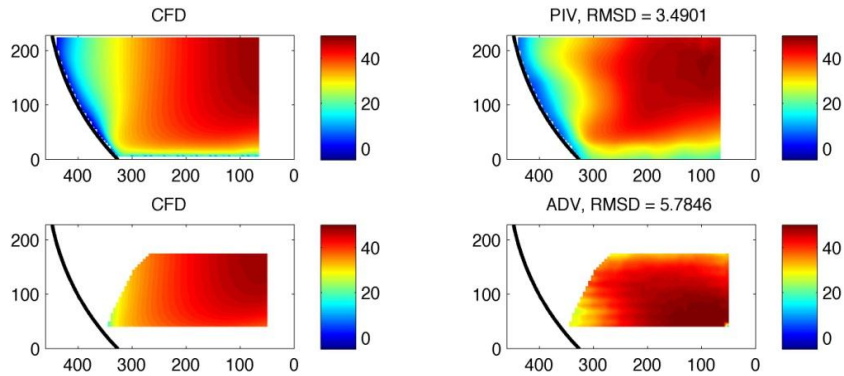

Figure 2.46: Comparison of the velocity distribution contour between CFD and PIV, CFD and ADV under the flow condition of 1.1fts and 9 inch water depth

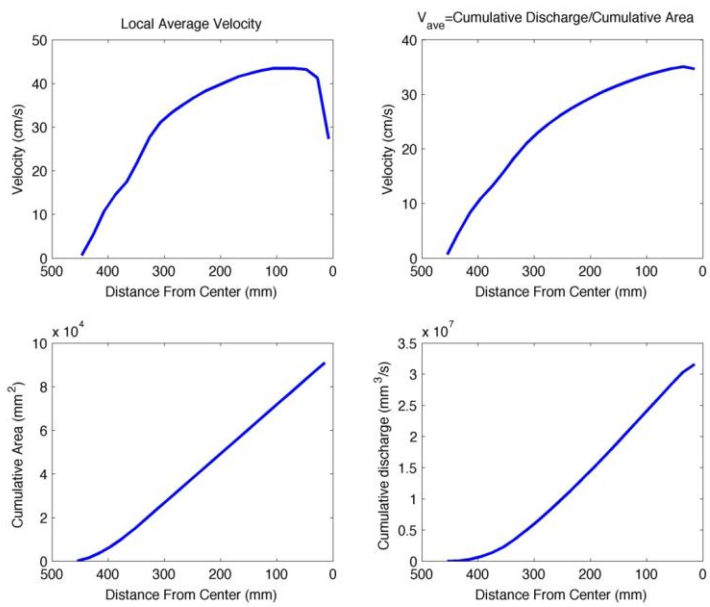

Figure 2.47: Depth-averaged velocity and cumulative average velocity curves development under the flow condition of 1.1fts and 9 inch water depth

2.4.1.4. Data process and error analyses

All original velocity data for each cell was exported and interpolated into uniform grids of 5 mm*5 mm in MATLAB. The PIV and ADV data can also be interpolated into uniform grids of 5 mm * 5 mm.

Here, we introduce an important variable called RMSD (root–mean–square deviation) to do the error analysis. The root–mean–square deviation (RMSD) is a frequently used measure of the difference between values predicted by a model or an estimator and the value actually observed from the thing being modeled or estimated. RMSD is a good measure of accuracy. These individual differences are also called residuals, and the RMSD serves to aggregate them into a single measure of predictive power *(http://en.wikipedia.org/wiki/Root_mean_square_deviation)*. Specifically, the RMSD is calculated by the function

RMSD= sqrt (mean(sum of the squares of errors between corresponding grids)).

Based on the 5mm *5 mm grids data, the RMSD were calculated for each case, and are listed in the Table 2.5 below. Note that differences in the PIV and ADV RMSD values calculated when comparing against CFD results indicate an uncertainty in experimental results that is of the same order of magnitude as the uncertainty as the CFD results.

Table 2.5: RMSD number between CFD and experimental data

Water depth (inch)	Velocity (fps)	PIV and CFD		ADV and CFD	
		RMSD	Relative error	RMSD	Relative error
4.5	0.71	2.4017	0.11	4.2799	0.20
6	0.71	4.532	0.21	4.3604	0.20
9	0.71	2.2145	0.10	3.8758	0.18
4.5	1.1	3.1694	0.09	6.258	0.19
6	1.1	4.749	0.14	7.3586	0.22
9	1.1	3.4901	0.10	5.7846	0.17

2.4.2. References

1. Matt Blank, Joel Cahoon, Tom McMahon, "Advanced studies of fish passage through culverts: 1-D and 3-D hydraulic modeling of velocity, fish expenditure and a new barrier assesment method," Department of Civil Engineering and Ecology, Montana State University, October, 2008.
2. Marian Muste, Hao-Che Ho, Daniel Mehl,"Insights into the origin & characteristic of the sedimentation process at multi barrel culverts in Iowa", Final Report, IHRB, TR-596, June, 2010.
3. Liaqat A. Khan, Elizabeth W.Roy, and Mizan Rashid, "CFD modelling of Forebay hydrodyamics created by a floating juvenile fish collection facility at the upper bank river dam", Washington, 2008.
4. Angela Gardner, "Fish Passage Through Road Culverts" MS Thesis, North Carolina State University, 2006.
5. Vishnu Vardhan Reddy Pati, "CFD modeling and analysis of flow through culverts", MS Thesis, Northern Illinois University, 2010.
6. Kornel Kerenyi, "Final Draft, Fish Passage in Large Culverts with Low Flow Proposed Tests" unpublished TFHRC experimental and CFD analysis of culvert flow for fish passage work plan, 2011.
7. CD-adapco, *User Guide STAR-CCM+ Version 6.04.014*, 2011

2.5. Modeling of Truck Generated Salt Spray under Bridge with Sliding Mesh

2.5.1. Model development

2.5.1.1. Geometry

In the previous quarter, a CFD approach to the modeling of truck generated salt spray was initiated. The technique of using a sliding mesh was employed to introduce movement of the vehicle. Domains with the truck and the bridge were separately built and meshed. A denser mesh with base size for an edge of 0.1 m was defined for the area surrounding the truck and the bridge beams. The rest of the domain was meshed with the base size of an element equal to 0.5 m. The geometry of the Raleigh - Tamarack Overpass (Bridge No. 4172) was used in the CFD analysis. In the base model the geometry of the embankment was not taken into account, the model represented a case where no obstructions on the side of the truck are present. In the recent quarter two more cases were analyzed: (1) with a wall boundary close to the truck and (2) with the realistic inclined embankment on the side of the truck as it passes under the bridge. With these cases, the tunneling effect can be investigated further. It was presented in the previous quarter that a single truck is not causing many droplets to be lifted up to the bridge beam level. For that reason, cases with two trucks traveling in one lane were considered. This is a more realistic case representing regular traffic conditions. Also, there were cases where the influence of the wind was analyzed. It was assumed that the most influential will be the wind blowing from the back at 45 degrees to the direction of travel (like shown in Figure 2.48)

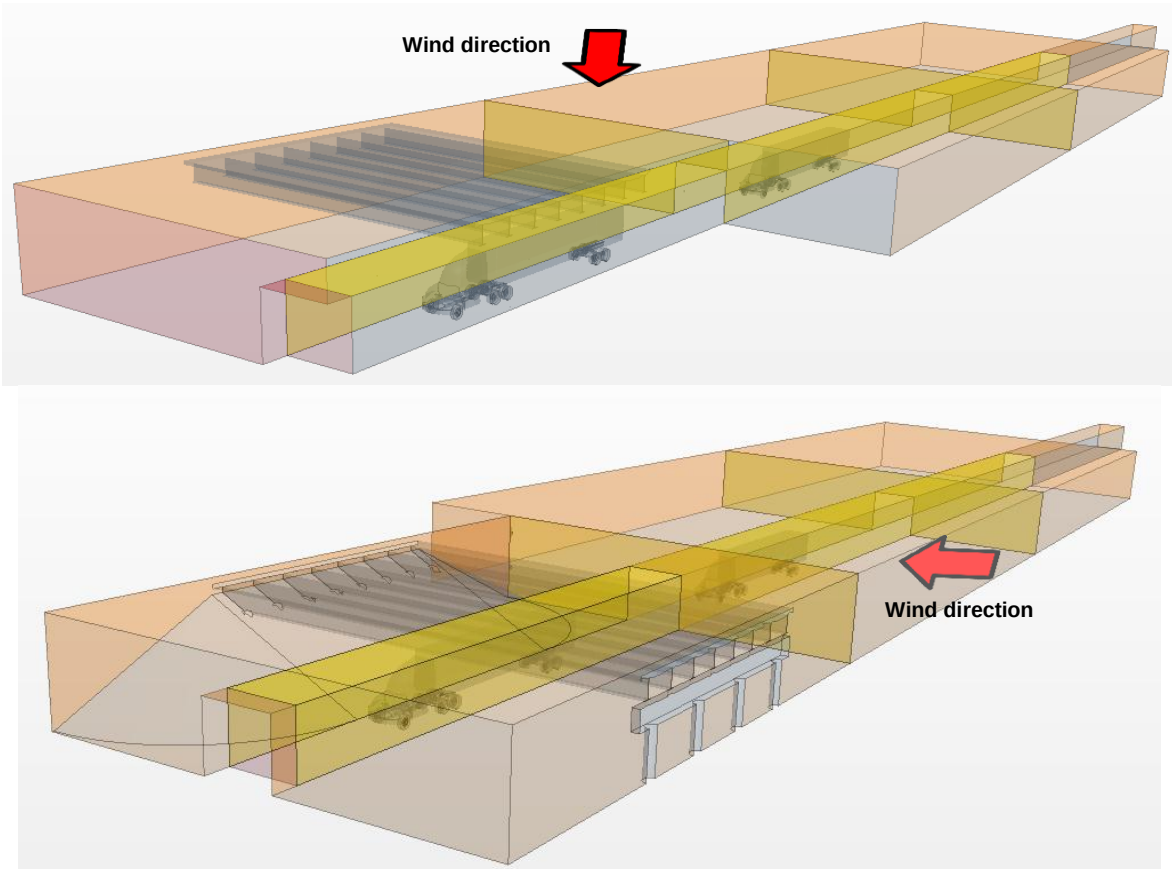

Figure 2.48: Two additional geometries of the bridge (top) close wall (bottom) inclined embankement

For both models the mesh settings were modified for the section with the bridge so the total number of cells was not greater than 4,000,000.

2.5.1.2. Spray generation

In the last quarter difficulties with estimating initial conditions regarding the spray generation on the tires were highlighted. The droplet size distribution, mass flow rate, direction and velocity of the generated spay were the most important parameters to be considered. The studies on spray generation performed at Lawrence Livermore National Laboratory (LLNL) were described briefly and reasoning for assumed initial conditions for our simulations was explained.

Set of simulations was started on a stationary vehicle, but oncoming air velocity of 60 mph, without the extended air domain and the bridge model. Of interest in this run was just the breakup of the droplets due to their impact with the wheel well. A goal of this simulation was to find what size droplets can be expected to leave the wheel well zone after the breakup. This size range is then used as a droplet injection boundary condition in the simulations of a moving vehicle, where it is too computationally expensive to use the breakup model. The Bai-Gosman wall impingement model was activated in these simulations. In the last quarter only results from one simulation were presented. In this quarter a whole matrix of simulations was performed for this part of the project and the results are presented below.

Two separate groups of simulations were performed with different angle of injection of the droplets relatively to the ground – 7.5 degrees and 15 degrees respectively. For both of these angles three different initial sizes of droplets were considered: 0.3 mm, 0.5 mm and 0.7 mm. These were representing the mean size of droplets generated in the experiments performed at LLNL. The simulations were run for 0.5 s and the mass flow rate of the spray was set to 4.5 kg/s following the LLNL findings.

Figure 2.49 shows final state of the simulations for the initial droplet size being 0.5 mm. Droplets are colored depending on their size with blue representing the smallest and red representing the biggest ones (with initial injection size). The red droplets behind the wheel didn't hit any elements of the wheel well and didn't break up. Although their trajectories look different in both cases (7.5 degrees and 15 degrees) the bulk of the smaller droplets leave the wheel well after the breakup to the side of it in a similar way for 7.5 degrees and 15 degrees cases.

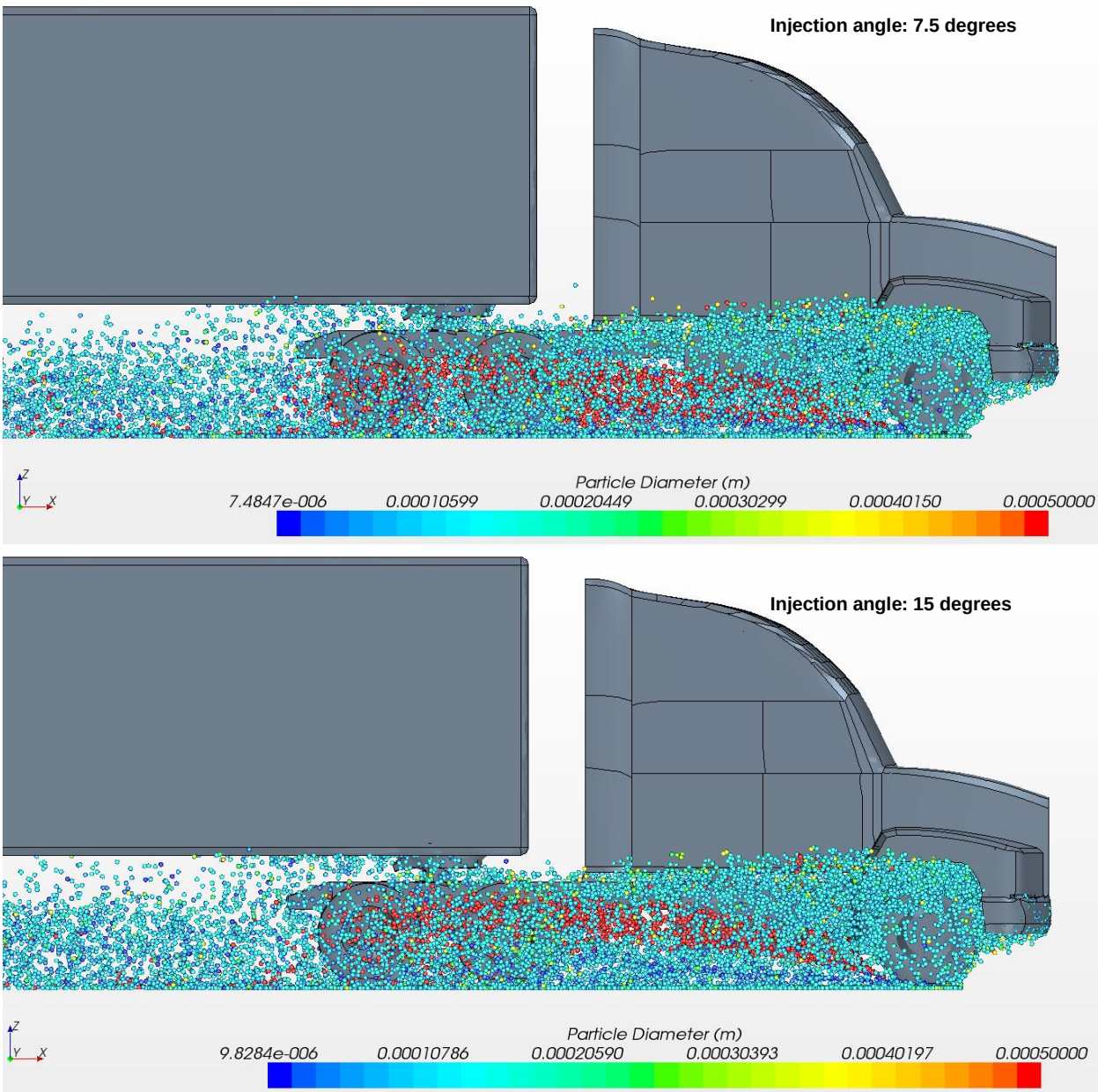

Figure 2.49: Droplet breakup in the wheel well (top) initial injection angle 7.5 degrees (bottom) initial injection angle 15 degrees

Figure 2.50 shows the distribution of the droplet sizes in the performed simulations. Comparing the corresponding results for injection angles 7.5 degrees and 15 degrees (left and right column) not much difference can be found. This initial angle was not relevant for the droplet size distribution. For different initial size of droplets different distributions were obtained. The highest counts were noted at around sizes 0.06 mm, 0.10 mm and 0.16 mm for the initial sizes 0.3 mm, 0.5 mm and 0.7 mm respectively. This study is in agreement with the assumed previously droplet size of interest between 0.025 mm and 0.2 mm. Droplets bigger than 0.2 mm diameter are not influenced much by the air flow and move following ballistic trajectories. However, smaller droplets in the micron size range are very likely to be suspended

in the air and may significantly influence the corrosion rate of the bridge beams. This part of the size spectrum was not analyzed here.

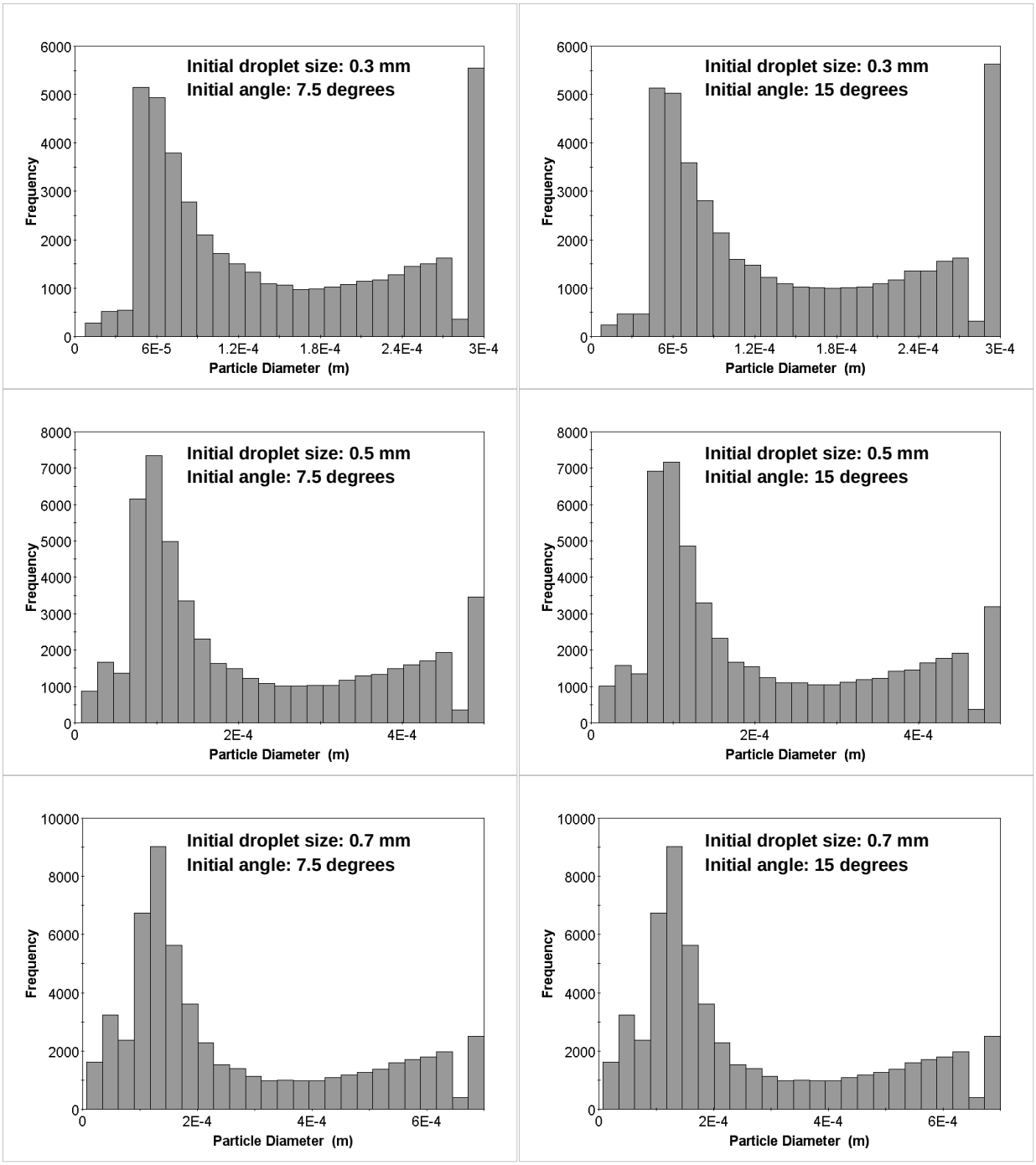

Figure 2.50: Droplet distribution after break-up in the wheel well

2.5.2. Simulations of the moving truck

As the main goal of this study is to provide an assessment of possible travel paths of a salt spray generated by the tires to the bridge beams, several cases were analyzed. In the previous quarter, cases with a single truck were analyzed. In all these cases not many droplets were moved to the beam level. In the recent quarter multiple cases with two trucks, one following another, were analyzed. Table 2.6 shows different parameters taken into account in the current matrix of simulations – four different droplet sizes, three different boundaries under the bridge, different wind conditions and different number of trucks. Since one simulation takes about 10 days of wall time, it is difficult to perform all the possible cases in a reasonable time. Not all the cases will be analyzed but at least for two sizes of droplets most of the possible cases will be simulated. In the recent quarter results for the droplet size of 0.05 mm are shown to establish a clearer picture of the up to date findings.

Table 2.6: List of analyzed cases

droplet sizes (mm)	0.01, 0.025, 0.05, 0.1
boundary types under the bridge	no boundaries, close wall, sloped embankment
wind conditions	no wind, wind from the back at 45° with 10 mph, 30 mph speed
number of vehicles	one, two

The number of droplet hits on the beams presented last time can lead to a misleading conclusion about the actual number of droplets making up to the level of the beams. Since the turbulent large field cannot be modeled exactly with a RANS model and the number of hits may be underrepresented it is better to show the distribution of the droplets' heights under the bridge. A sampling volume was built for each case bounded by the extent of the bridge and a plane cutting the vehicle through the middle of it. The distribution at four different stages of the simulation are calculated:

- At 4.0 sec – when the first vehicle is under the bridge
- At 5.0 sec – when the first vehicle leaves the underpass
- At 5.5 sec – when the second vehicle is under the bridge
- At 6.0 sec – when the second vehicle leaves the underpass.

Figure 2.51 through Figure 2.56 show the distribution of the droplets for the different boundary and wind conditions. In red and orange color are shown bars representing droplets making it up to the level of the beams. Red bars indicate droplets that are up between the beams, and orange bars indicate droplets that are within 0.25 m of the bottom of the beams. The bottom flange of the bridge beam is located at 5.5 m and the bottom surface of the deck is located at 6.9 m. Droplets in between that range may contribute to the salt spray deposition on the elements of the bridge. Interesting is the fact that for the case with the wall there are considerably fewer droplets at the beam level (Figure 2.52) than for the case with open boundaries (Figure 2.51). For the case with the high velocity wind this number drops even more (Figure 2.53). The droplets are transported by the wind from underneath the bridge outside of that part of domain. Surprising is the fact that for the case with the slope a lot more droplets make it above the 5.5 m level (Figure 2.54). The wind of 10 mph speed does not make much of a difference in this distribution (Figure 2.55). However, high velocity wind of 30 mph increases considerably the number of droplets making it up to the beam levels (Figure 2.56). Wind frequent gusts of up to 30 mph were considered a likely but near maximum wind speed for winter storms or windy days in which the average wind speed is between 15 and 20 mph.

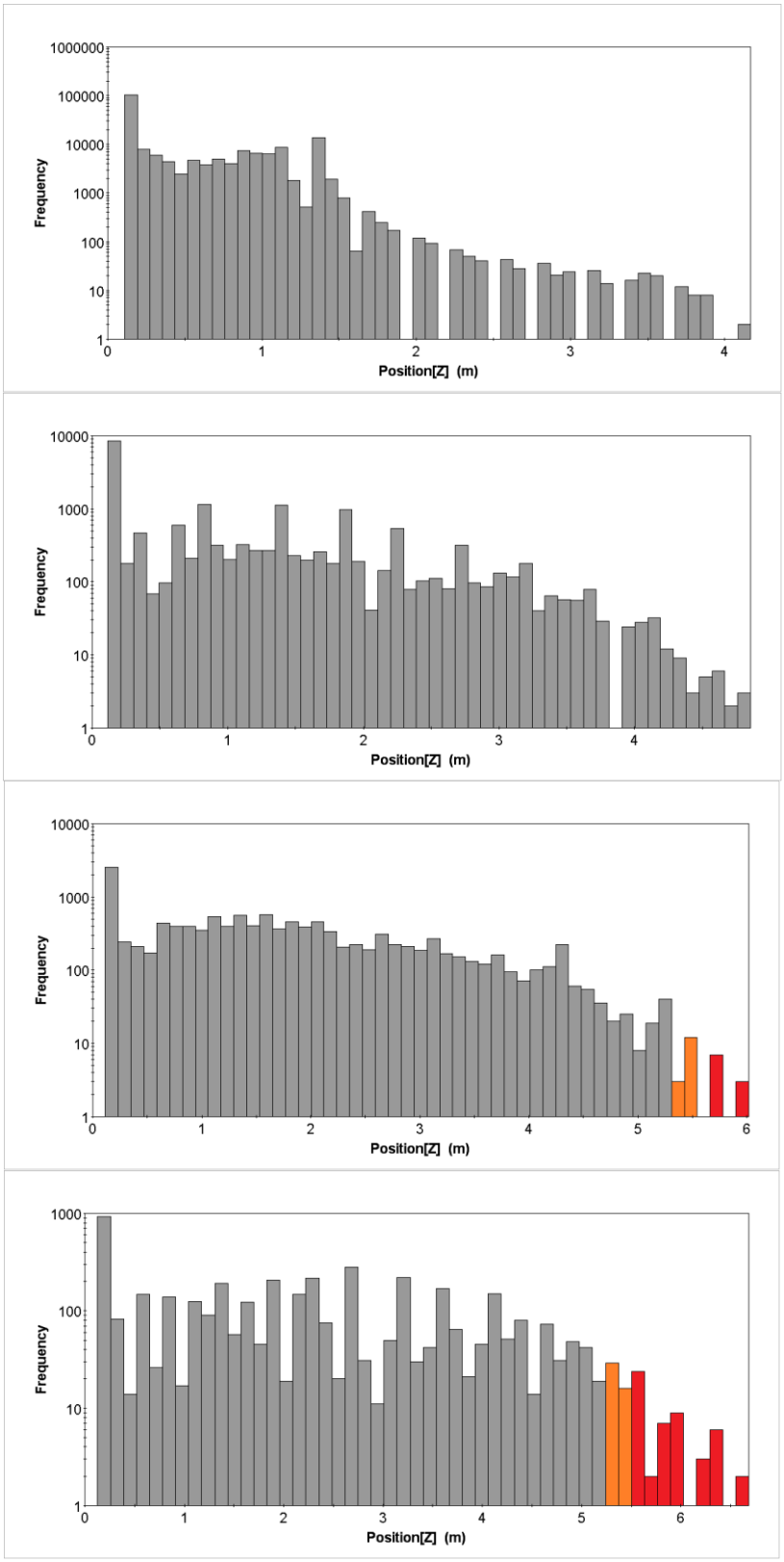

Figure 2.51: Droplet distribution in the volume under the bridge for initial model (no boundaries, no wind) at: (a) 4.0 sec (b) 5.sec (c) 5.5 sec (d) 6.5 sec

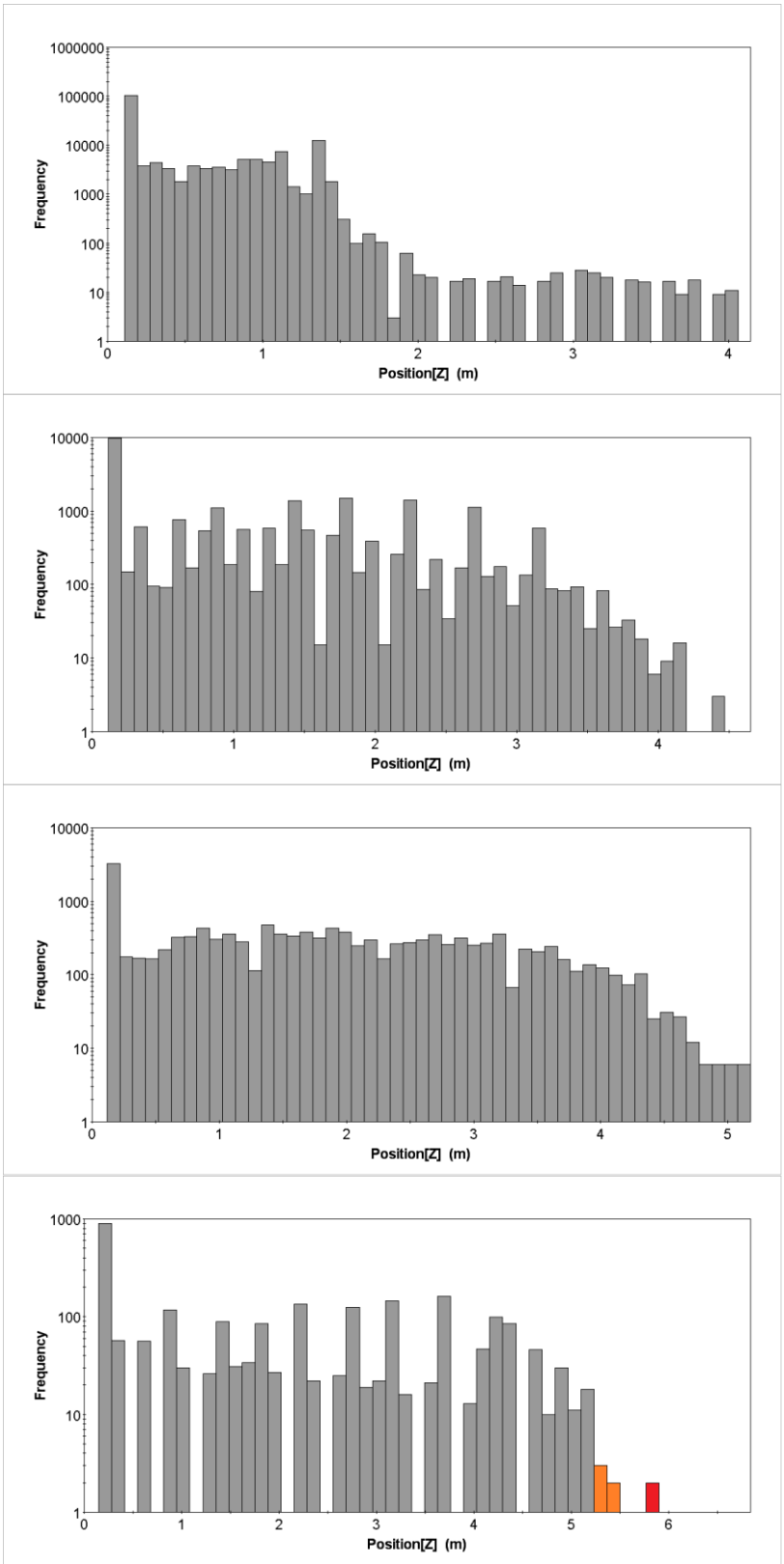

Figure 2.52: Droplet distribution in the volume under the bridge for the model with the wall, no wind at: (a) 4.0 sec (b) 5.0 sec (c) 5.5 sec (d) 6.5 sec

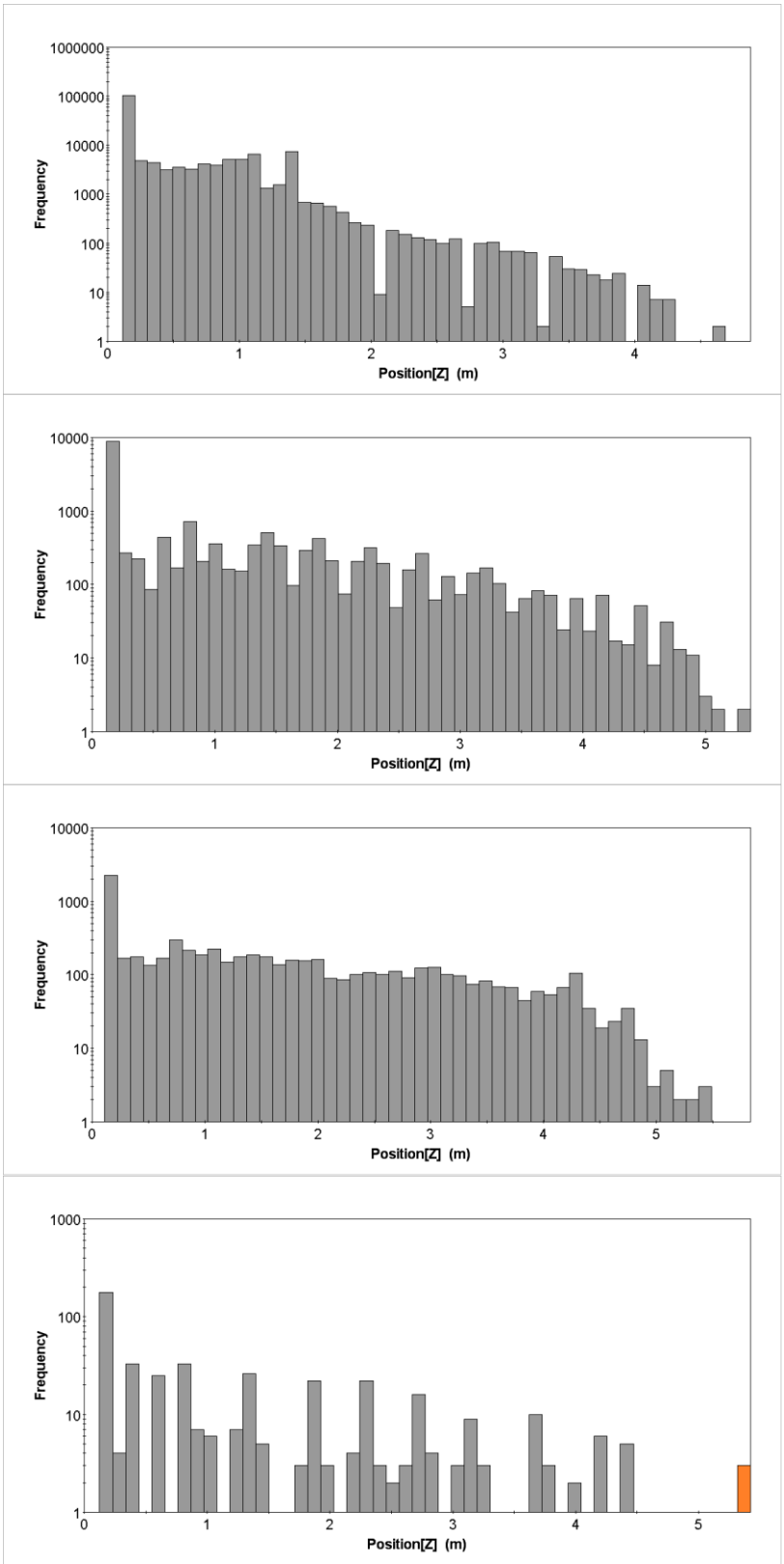

Figure 2.53: Droplet distribution in the volume under the bridge for the model with the wall and 30 mph wind at: (a) 4.0 sec (b) 5.0 sec (c) 5.5 sec (d) 6.5 sec

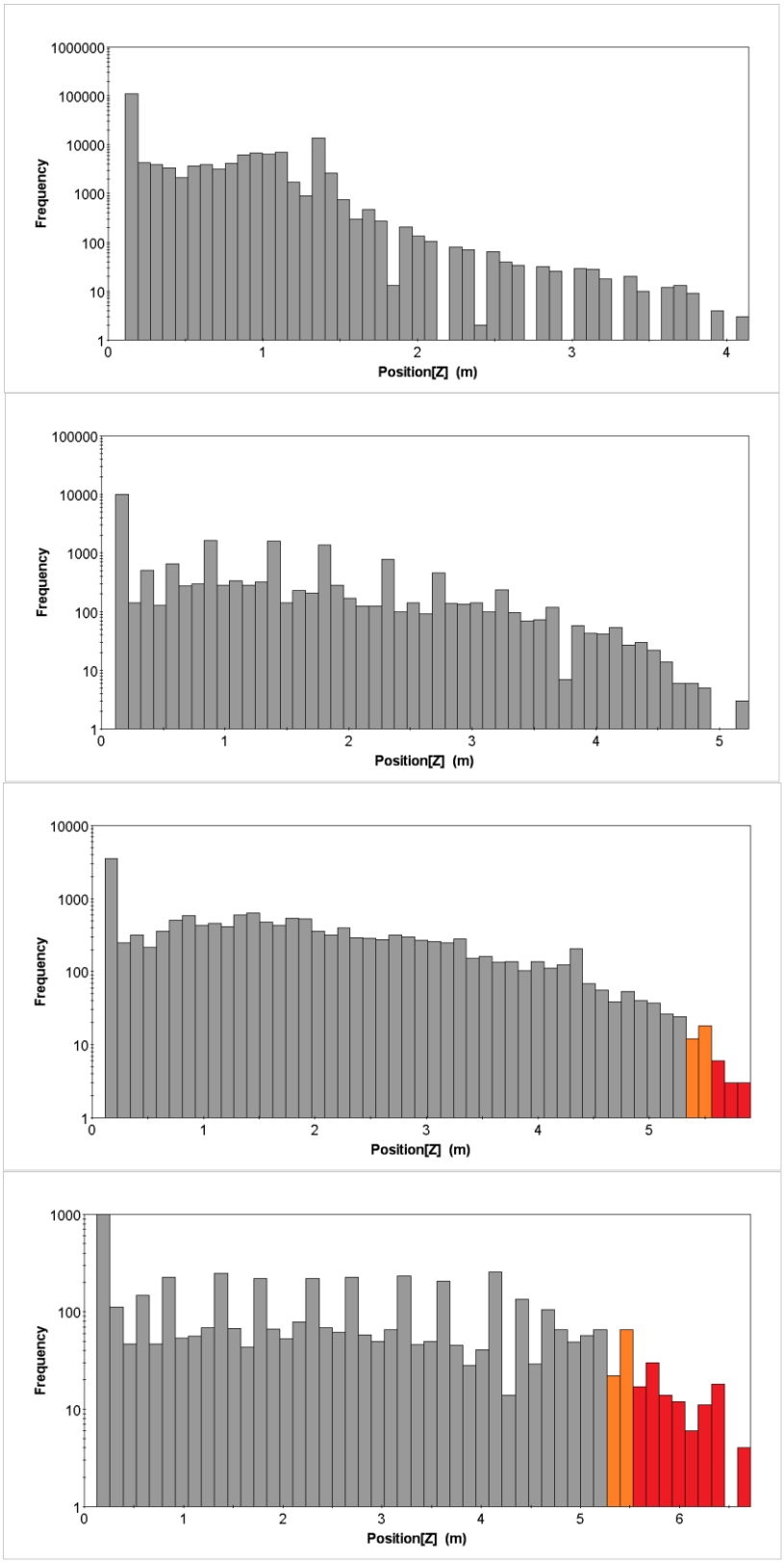

Figure 2.54: Droplet distribution in the volume under the bridge for the model with sloped embankment and no wind at: (a) 4.0 sec (b) 5.0 sec (c) 5.5 sec (d) 6.5 sec

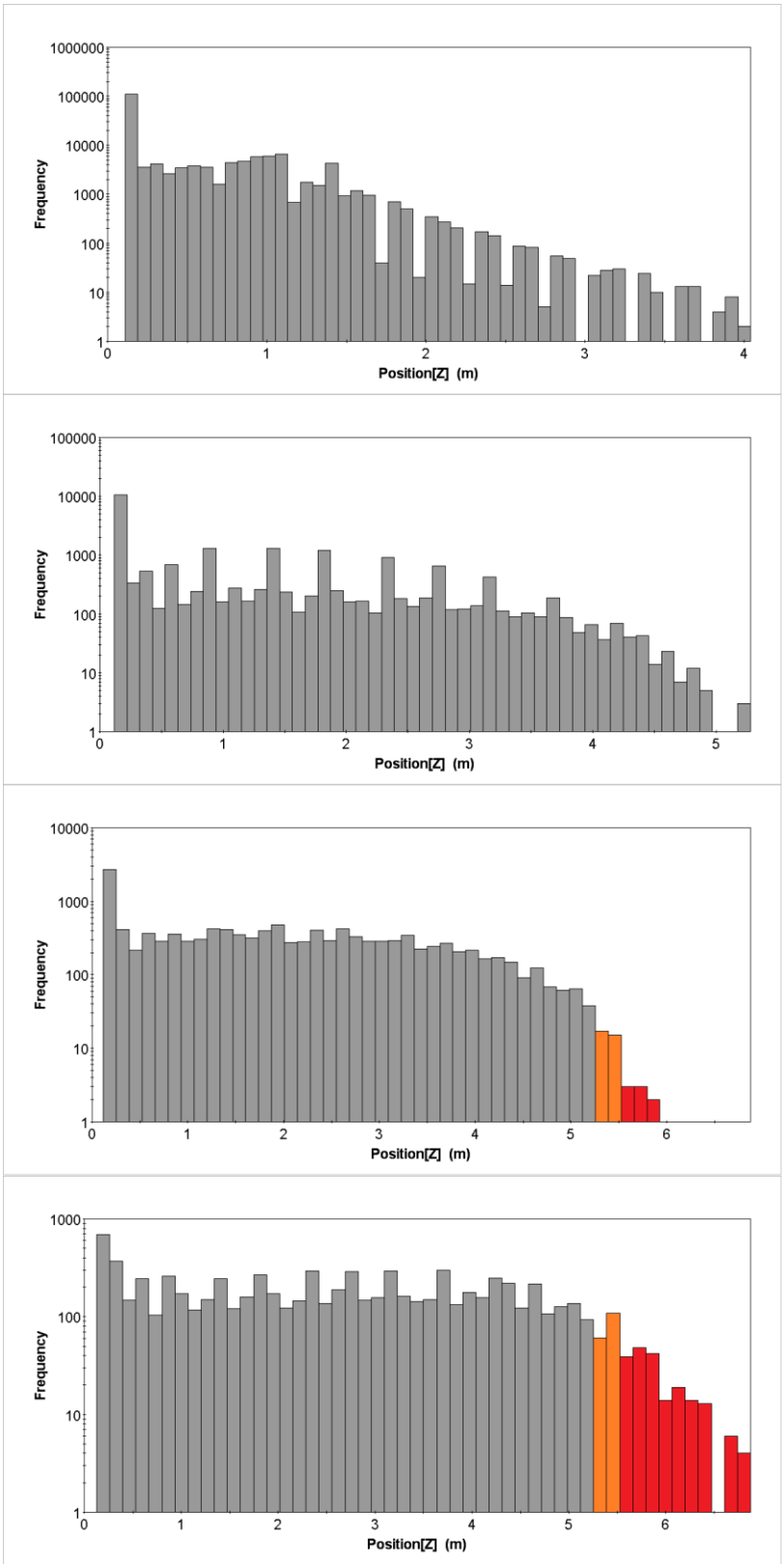

Figure 2.55: Droplet distribution in the volume under the bridge for the model with sloped embankment and 10 mph wind at: (a) 4.0 sec (b) 5.0 sec (c) 5.5 sec (d) 6.5 sec

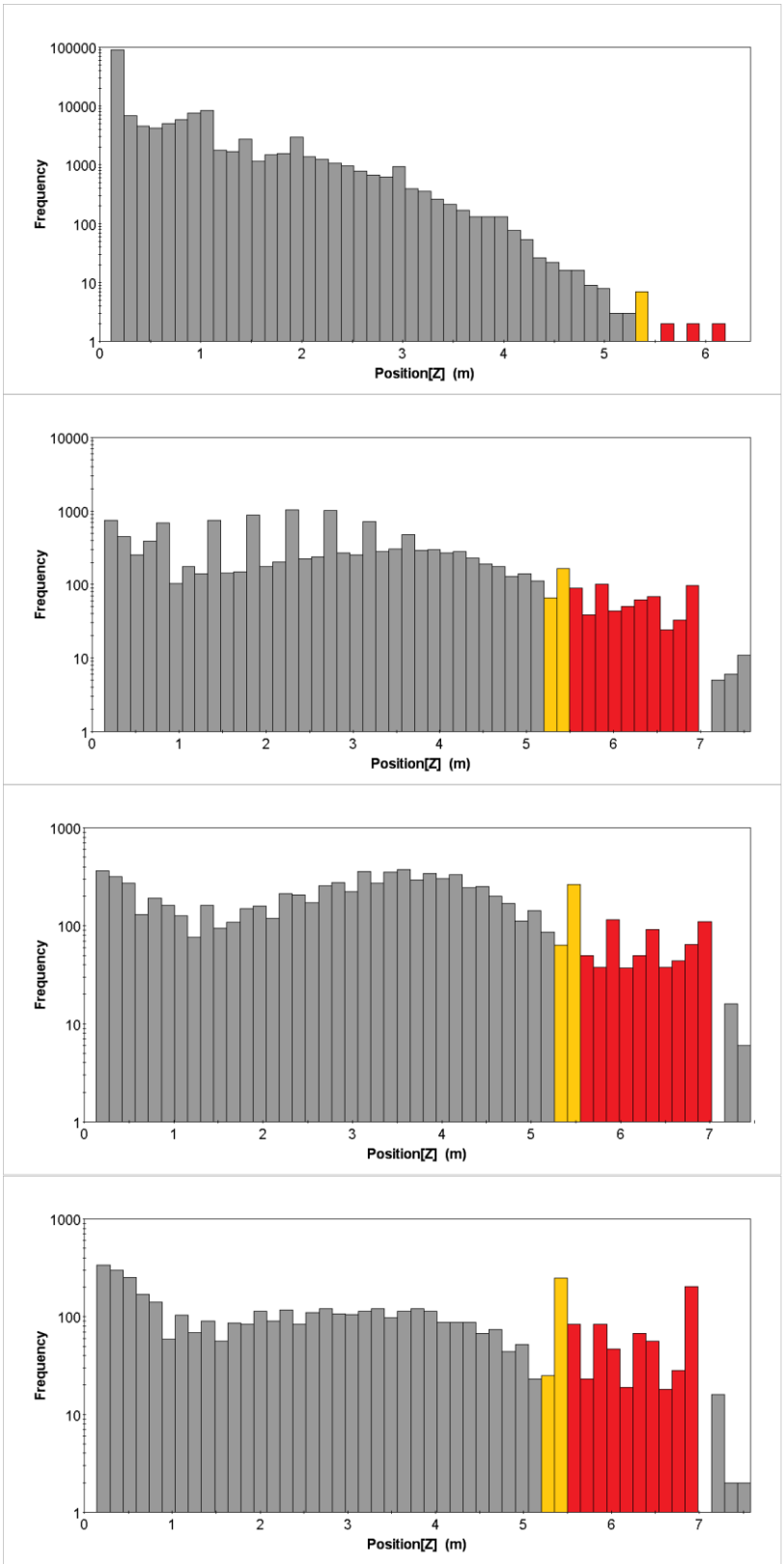

Figure 2.56: Droplet distribution in the volume under the bridge for the model with sloped embankment and 30 mph wind at: (a) 4.0 sec (b) 5.0 sec (c) 5.5 sec (d) 6.5 sec

Figure 2.57 through Figure 2.60 show the velocity vector plots under the bridge for different boundary conditions under the bridge. These plots may actually explain why for the case with the sloped embankment we see the biggest number of droplets traveling to the beam level. Figure 2.57 shows velocity vectors at four different time frames (4.0. sec, 5.0 sec, 5.5 sec and 6.5 sec) for the initial model without obstructions underneath the bridge. Figure 2.58 is for the case with the wall and lateral wind. Once the second truck leaves this cross section the wind dominates the flow. There are no vortices that could possibly transport the droplets up to the beams. The situation is quite different for the cases with the sloped embankment presented in Figure 2.59 and Figure 2.60. On the surface of the slope there are recirculation zones forming. Large vortices are created that may transport droplets up to the level of the beams.

In the next quarter the matrix of the simulations will be expanded to more cases and the droplet distributions will be plotted for further stages of the simulations i.e. 8.0 sec and 10 sec when all the droplets leave the bridge area.

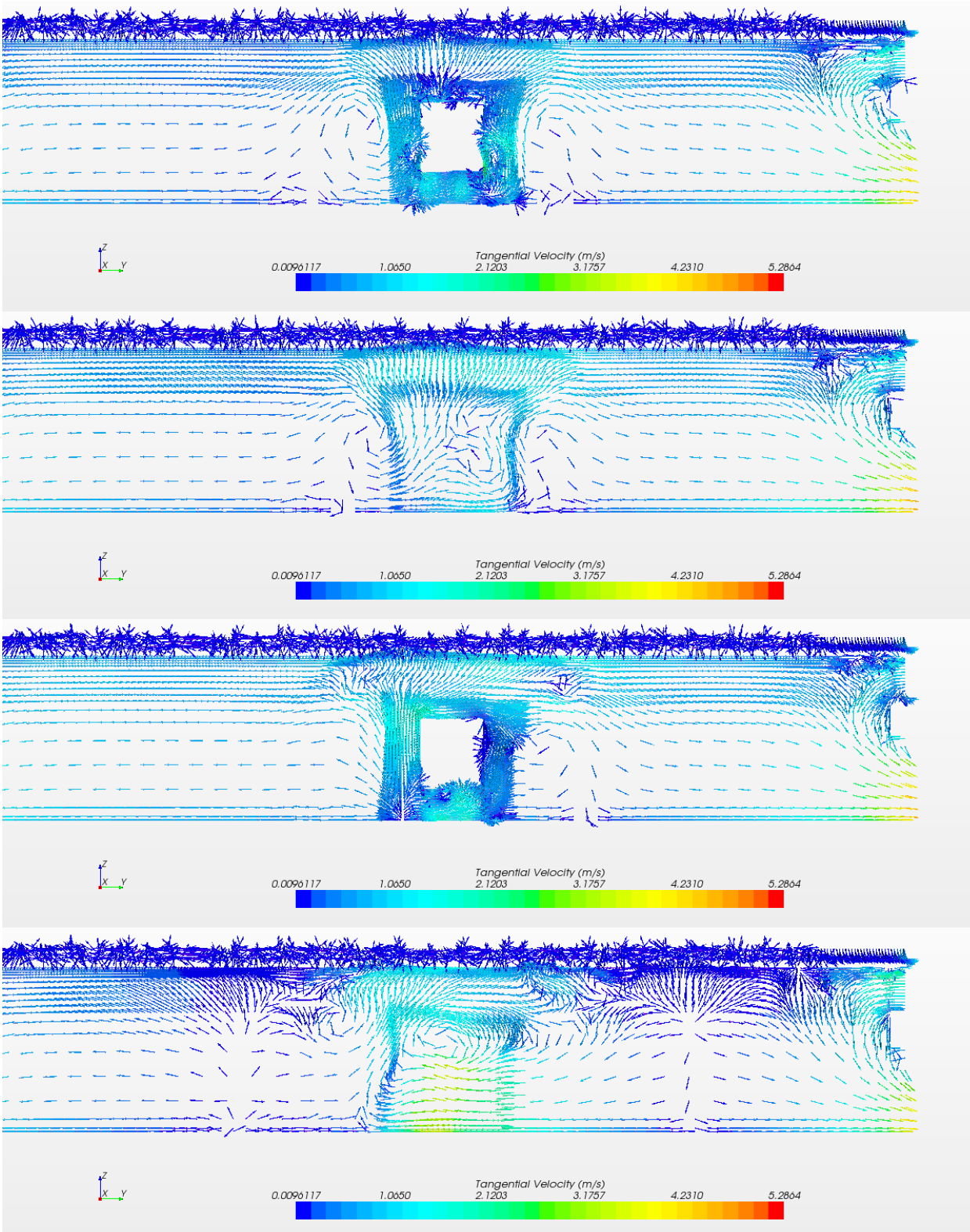

Figure 2.57: Velocity vector plot under the bridge in the initial model (no boundaries, no wind) at: (a) 4.0 sec (b) 5.0 sec (c) 5.5 sec (d) 6.5 sec

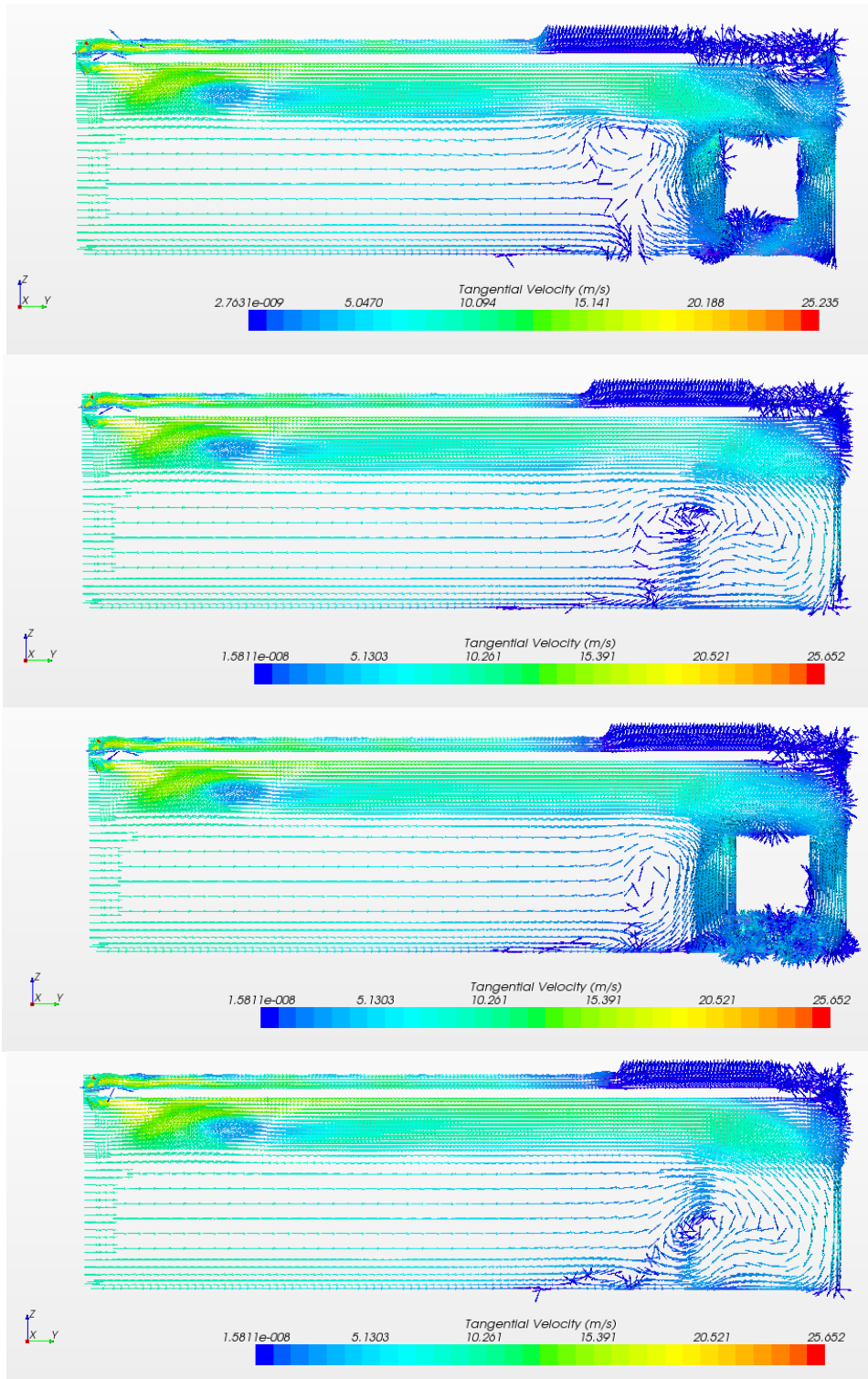

Figure 2.58: Velocity vector plot under the bridge in the model with the wall and 30 mph wind at: (a) 4.0 sec (b) 5.0 sec (c) 5.5 sec (d) 6.5 sec

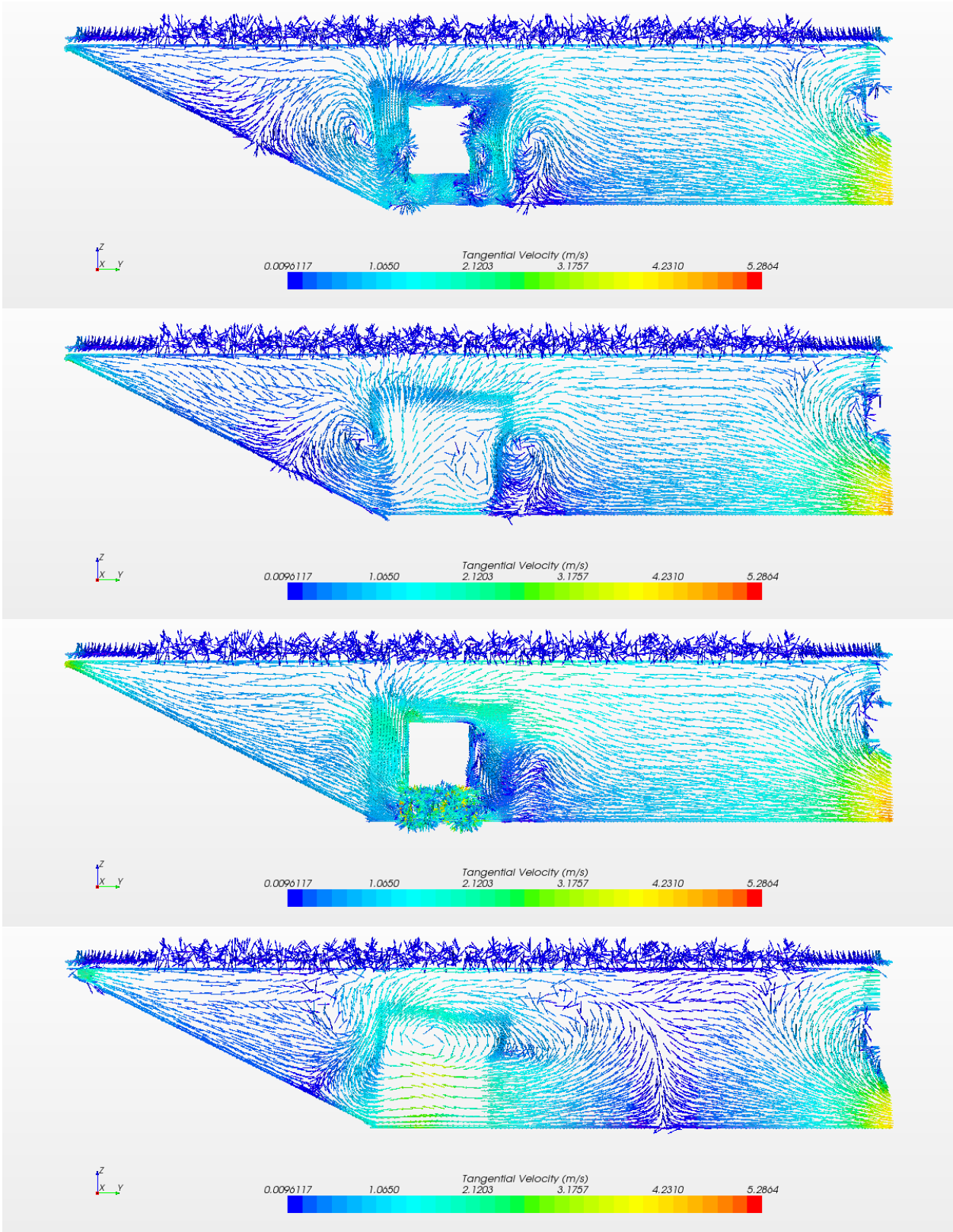

Figure 2.59: Velocity vector plot under the bridge for the model with sloped embankment and no wind at: (a) 4.0 sec (b) 5.0 sec (c) 5.5 sec (d) 6.5 sec

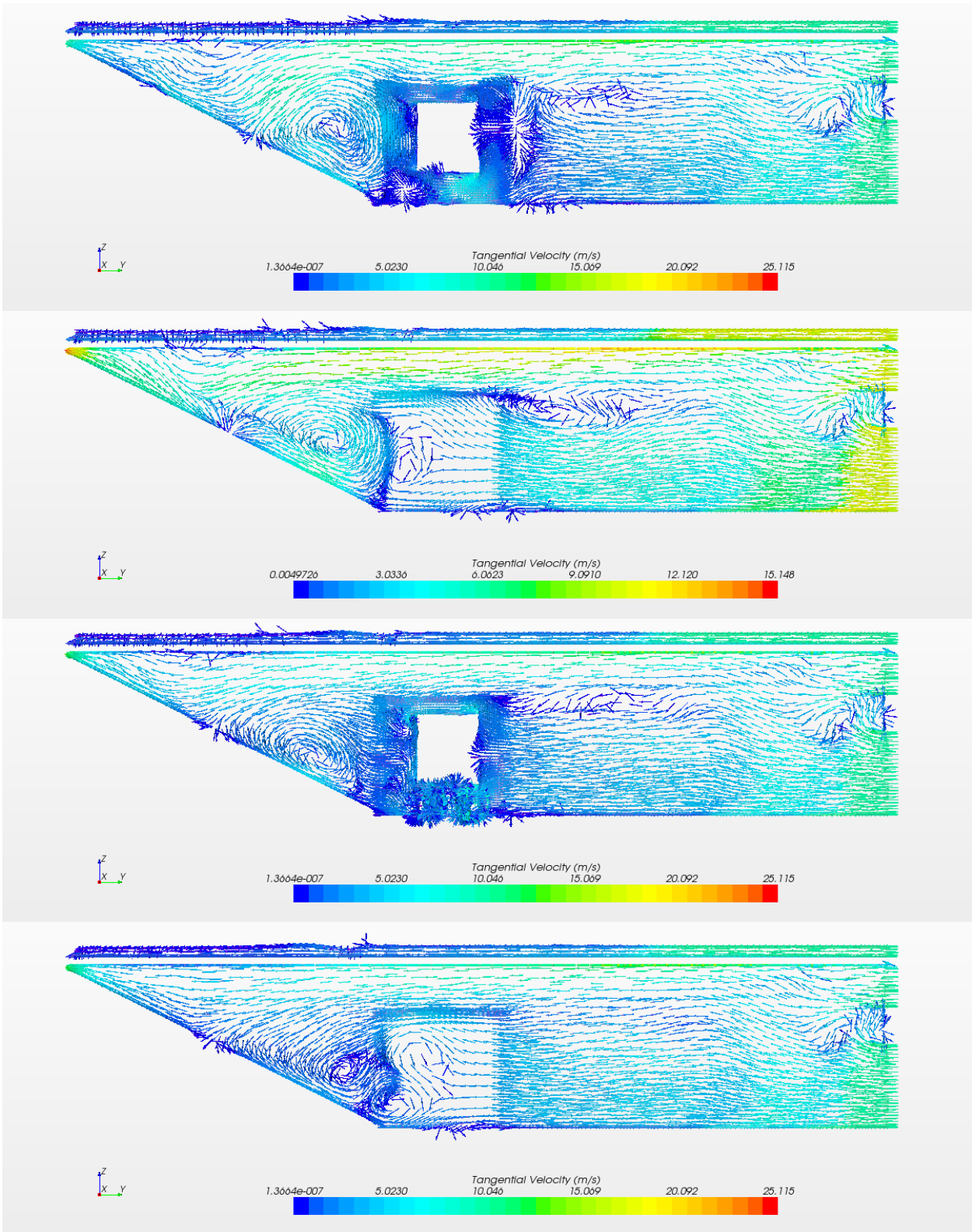

Figure 2.60: Velocity vector plot under the bridge for the model with sloped embankment and 30 mph wind at: (a) 4.0 sec (b) 5.0 sec (c) 5.5 sec (d) 6.5 sec

Energy Systems Division
Argonne National Laboratory
9700 South Cass Avenue, Bldg. 362
Argonne, IL 60439-4815

www.anl.gov

Argonne National Laboratory is a U.S. Department of Energy
laboratory managed by UChicago Argonne, LLC